CeO_2-Modified Bimetallic Sulfides for Efficient Energy Storage in Supercapacitors: A Comparative study of ZnCoS and CuCoS

Sina Maghool[a], *Ali Akbar Asgharinezhad*[b,*], *Zeynab Molaei*[a], *Afsanehsadat Larimi*[c,*], *Cyrus Gotbi*[a]

[a] Department of Chemical and petroleum Engineering, Sharif University of Technology, Tehran, Iran.

[b] Chemistry and Process Research Department, Niroo Research Institute, Tehran, Iran.

[c] School of Engineering and Applied Sciences, Department of Chemical Engineering, Swansea University, Wales, UK.

*Corresponding authors' Email: aasgharinezhad@nri.ac.ir (A. A. Asgharinezhad);

a.larimi@swansea.ac.uk (A. Larimi)

Tel: +9888079400

Abstract

Supercapacitors have emerged as efficient energy-storage systems due to their high output power, rapid charging/discharging capability, and long cycle life, making them suitable for applications ranging from portable electronics to electric vehicles. This paper presents the fabrication and electrochemical performance of bimetallic sulfide structures combined with cerium oxide (CeO_2) nanosheets for supercapacitor applications. $ZnCoS/CeO_2$ and $CuCoS/CeO_2$ electrodes were prepared through a sulfidation process, followed by analysis of their architecture and electrochemical behavior. A key novelty of this work is the direct comparison of Zn- and Cu-based CeO_2-integrated bimetallic sulfide electrodes within the same synthesis and testing framework, enabling identification of the role of metal selection in electrochemical performance. Analyses confirmed successful incorporation of CeO_2 nanosheets and the formation of uniform bimetallic sulfide frameworks. Electrochemical evaluation was carried out using a three-electrode setup. The $ZnCoS/CeO_2$ electrode achieved a high specific capacitance of 616.25 F g^{-1} at 1 A g^{-1}, significantly surpassing the $CuCoS/CeO_2$ counterpart, which delivered 416.25 F g^{-1}. This improvement is attributed to the synergistic effect of CeO_2 nanosheets and Zn, which improves charge-transfer behavior and ion/electron transport. The $ZnCoS/CeO_2$ and $CuCoS/CeO_2$ electrodes retained 86.7% and 86% of their initial capacitance after 2500 cycles, respectively. Asymmetric supercapacitors using $ZnCoS/CeO_2$ and $CuCoS/CeO_2$ as cathodes and activated carbon as the anode showed significant energy-storage potential. These results highlight the promise of $CeO_2$2-integrated bimetallic sulfide structures for advanced energy-storage applications.

Keywords: Supercapacitor; Energy storage; CeO_2 nanosheets; Zinc-cobalt sulfide, Copper-cobalt sulfide; Power density.

1. Introduction

Today, the primary sources of energy supply are fossil fuels such as coal, diesel, and petrol, which pose serious environmental risks such as increased greenhouse gases and global warming [1,2]. In addition to the environmental impacts of fossil fuels, a significant amount of time is needed to replace these resources [3]. Therefore, considering the increasing demand for energy, renewable energies have gained attention as they are both clean and inexhaustible [4–6]. However, the energy produced from renewable sources is intermittent and requires energy storage system [7,8]. Fuel cells, rechargeable cells, and supercapacitors rank among the key energy conversion technologies and have shown high efficiency in modern energy storage systems [9,10]. Supercapacitors have garnered significant attention for bridging the gap between the limited energy storage of traditional capacitors and the restricted power output typically associated with fuel cells and rechargeable batteries [11–13]. Its high-power density, extended cycle life, and quick charging and discharging speed make it ideal for a variety of uses, uninterruptible power supply (UPS), flexible displays, and wearable technology [14–16].

Cerium oxide (CeO_2) is regarded as a viable candidate for supercapacitor applications due to its environmental friendliness, non-toxicity, availability, cheaper cost among rare earth elements, and existence of oxygen vacancies [17,18]. Also, Ce has two oxidation states, trivalent and tetravalent, that transition between these states results in a fast redox reaction in cerium and the electrolyte, thereby helping to improve electrochemical performance [19,20]. However, lattice expansion due to the conversion of Ce^{3+} to Ce^{4+} results in insufficient structural stability [21]. In addition, the low conductivity of CeO_2, as a semiconductor, results insufficient specific capacitance [22–24]. Therefore, it is preferred not to be used alone but rather in hybrid or composite forms [25,26]. For instance, Mazloom et al. [27] made a core-shell structured α-Fe_2O_3@CeO_2 and reported its specific

capacitance at 5 mV s^{-1} to be 168 F g^{-1}. Xiao et al. [28] synthesized MWCNTs@CeO_2 via a solvothermal approach, achieving a capacitance performance of 421.1 F g^{-1} when tested under a current density of 1 A g^{-1}.

According to the disparity in energy levels between O 2p and S 2p orbitals, coupled with sulfur's lower electronegativity relative to oxygen, transition metal sulfides frequently exhibit superior conductivity in comparison to oxides, making them exceptional candidates for battery materials [29,30]. In comparison to their corresponding oxides and hydroxides, transition metal sulfides offer enhanced electrical conductivity, improved structural integrity, better thermal resistance, extended durability, and greater theoretical capacitance [31,32].

Moreover, sulfide form of transition metals are among the best options as supercapacitors due to their outstanding capacity, abundance, low cost, compatibility with the environment, and rich redox, in addition to the previously listed benefits [33–35]. Among transition metal sulfides, bimetallic sulfides are preferred over monometallic sulfides due to their synergistic effect, multiple oxidation sites, and improved electrical conductivity. They possess richer and more stable electrochemical activity [36–38]. Recently, bimetallic sulfides containing cobalt as one of the metals, such as $ZnCo_2S_4$ [39] and $CuCo_2S_4$ [40], have gained attention because cobalt improves electrical conductivity and consequently enhances supercapacitor performance [41].

In this study, CeO_2-integrated cobalt-based bimetallic sulfide composites were developed as supercapacitor electrodes through a three-step route involving CeO_2 nanosheet formation, growth of MCo LDH precursors (M = Zn, Cu), and subsequent sulfidation to obtain MCoS/CeO_2 structures. Unlike many previous reports that focus on a single sulfide composition or a single composite design, the present work provides a direct comparative investigation of two related systems, ZnCoS/CeO_2 and CuCoS/CeO_2, in order to clarify the influence of metal selection

together with CeO_2 incorporation on structural evolution and electrochemical behavior. The novelty of this work lies in combining CeO_2 nanosheets with two cobalt-based bimetallic sulfides within the same experimental framework and systematically evaluating the roles of sulfidation, CeO_2 integration, and cation type in determining capacitance, resistance, and device-level performance. The results reveal that ZnCoS/CeO_2 delivers the best overall electrochemical response, achieving 616.25 F g^{-1} at 1 A g^{-1}, lower internal resistance than the comparison electrodes, and an asymmetric-device energy density of 22 Wh kg^{-1} at 640 W kg^{-1}, thereby identifying Zn-based CeO_2-integrated bimetallic sulfide as the more effective configuration in the present system.

2. Experimental part

2.1. Materials

Copper(II) nitrate trihydrate ($Cu(NO_3)_2{\cdot}3H_2O$), cobalt(II) nitrate hexahydrate ($Co(NO_3)_2{\cdot}6H_2O$), zinc(II) nitrate tetrahydrate ($Zn(NO_3)_2{\cdot}4H_2O$), cerium(III) nitrate hexahydrate ($Ce(NO_3)_3{\cdot}6H_2O$), ammonium fluoride (NH_4F), sodium hydrogen carbonate ($NaHCO_3$), carbon black (C), potassium hydroxide (KOH), ethanol (C_2H_6O), acetone (C_3H_6O), hydrochloric acid (HCl), *N*-methyl-2-pyrrolidone (C_5H_9NO), and urea ($CO(NH_2)_2$) were purchased from Merck (Germany). Sodium sulfide hydrate (Na_2S) was obtained from Acros Organics Co (Belgium). Polyvinylidene fluoride was sourced via Alfa Chemistry (USA). Nickel foam (NF), 0.3 mm thick, was acquired through American Elements (USA). Methanol (CH_3OH) was supplied by Neutron Pharmacochemical Co. (Iran).

2.2. Fabrication of CeO_2 nanosheets

The materials were prepared following the procedure illustrated in Scheme 1. To synthesize CeO_2 nanosheets, specific amount of $Ce(NO_3)_3 \cdot 6H_2O$ (2.78 g) and 1.594 g of $NaHCO_3$ were individually dispersed in water (50 ml) via ultrasonic agitation. These solutions were then mixed and stirred at 30 °C for 24 h by employing a magnetic stirrer. The resulting solid was washed using distilled water and then subjected to drying at 80 °C in an oven for a duration of 15 h. Ultimately, cerium oxide nanosheets were acquired by calcining the precipitate for 4 h at 500 °C.

2.3. Synthesize of MCo LDH/CeO_2 (M = Zn, Cu) and MCo LDH (M = Zn, Cu)

To produce ZnCo LDH/CeO_2, 0.339 g of generated CeO_2 nanosheets were dispersed in 50 ml of water using ultrasonic treatment. Then, 2.328 g of $Co(NO_3)_2 \cdot 6H_2O$, 1.045 g of $Zn(NO_3)_2 \cdot 4H_2O$, 0.148 g of NH_4F, and 0.961 g of $CO(NH_2)_2$ were included into the solution of CeO_2 nanosheet. The mixture was agitated for 30 minutes with a magnetic stirrer and then placed in an autoclave, maintained at 90 °C for 24 h. The resulting material underwent successive rinsing steps using ethanol followed by purified water to remove any residual impurities. After the cleaning process, the sample was subjected to thermal treatment at 80 °C for 12 h to ensure complete drying.

In the synthesis of CuCo LDH/CeO_2, all preceding steps were replicated, with the exception that 0.966 g of $Cu(NO_3)_2 \cdot 3H_2O$ was utilized in place of $Zn(NO_3)_2 \cdot 4H_2O$. Furthermore, to further the comparability of the structures, ZnCo LDH and CuCo LDH were synthesized using the identical process, excluding the addition of cerium oxide.

2.4. Synthesize of MCoS/CeO_2 (M = Zn, Cu) and MCoS (M = Zn, Cu)

To synthesize the sulfide structures, 0.2 g of ZnCo LDH/CeO_2, CuCo LDH/CeO_2, ZnCo LDH, and CuCo LDH was introduced into 50 ml of 0.1 M Na_2S aqueous medium, and then it was subjected to ultrasonic waves for 10 min. Afterward, the reaction solution was placed into 100 ml autoclaves

lined with Teflon and maintained at 120 °C over an 8-hour period. final solid product underwent triple rinsing with ethanol followed by another three washes using distilled water, and was subsequently oven-dried at 80 °C for 16 h.

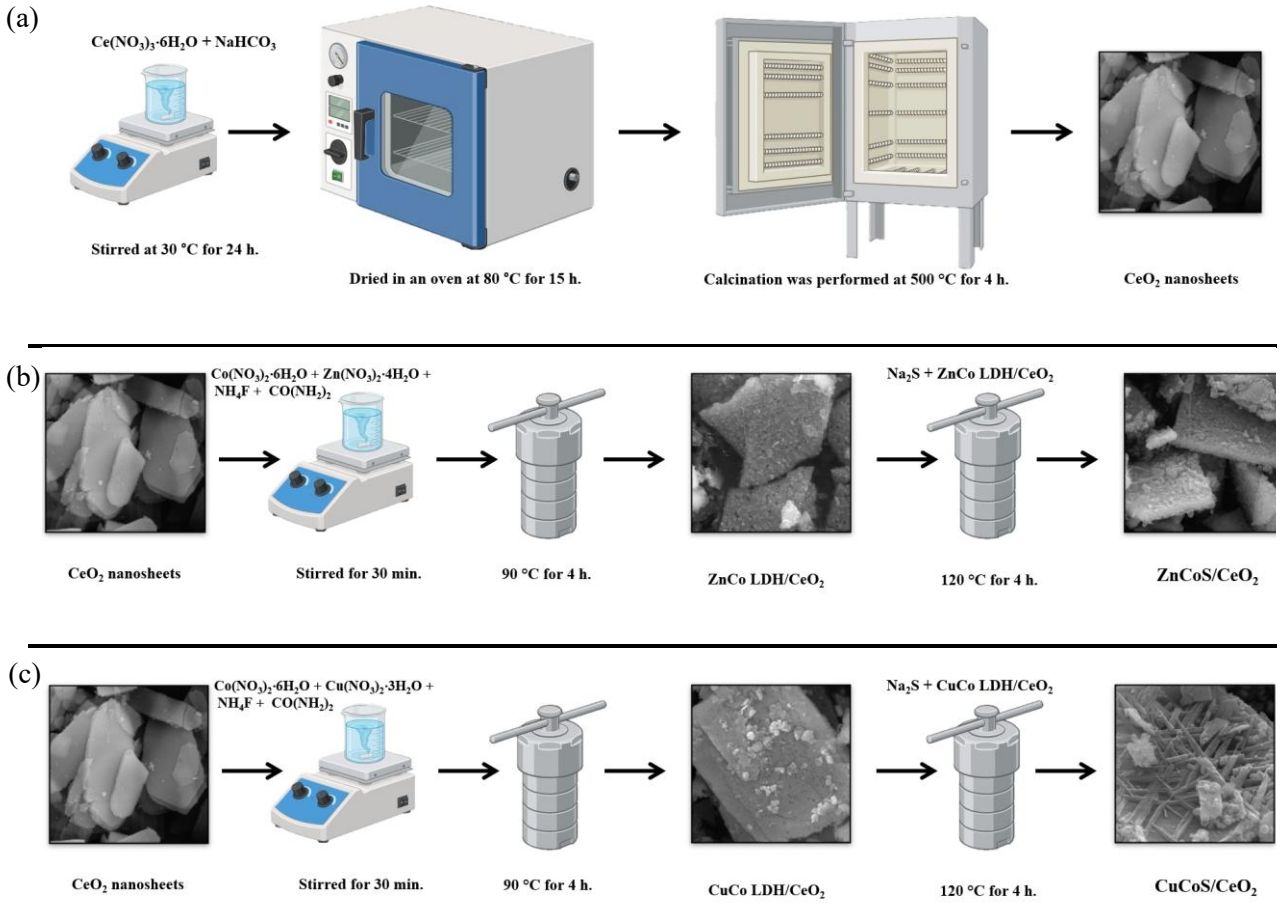

Scheme 1. Illustration depicting the synthesis process of (a) CeO_2, (b) ZnCo LDH/CeO_2 and ZnCoS/CeO_2, (c) CuCo LDH/CeO_2 and CuCoS/CeO_2.

2.4. Materials characterization

The structural composition of the synthesized materials was examined using diffraction analysis techniques. Specifically, phase identification was carried out using a PANalytical XPert PRO MPD system (UK) based on XRD methodology. Sample morphology was analyzed through field

emission scanning electron microscope (FE-SEM) imaging performed with a TESCAN MIRA 3 LMU instrument manufactured in the Czech Republic. A TESCAN (MIRA 3 LMU) equipment from the Czech Republic was used to assess the elemental chemical properties by energy dispersive spectroscopy (EDS). Detailed morphological analysis at the nanoscale was carried out by employing a Zeiss EM10C-100Kv system (Germany), which utilizes transmission electron microscopy (TEM) for high-resolution imaging. Elemental composition and valence state information were also determined using a Kratos Axis Supra X-ray Photoelectron Spectrometer (XPS), Japan.

2.5. Electrochemical measurement

A Palmsens 4 device was utilized for electrochemical studies, with all measurements performed in a 3 M KOH electrolyte. An electrochemical cell consisting of three electrodes was employed: Ag/AgCl served as the reference, platinum wire acted as the counter, and the working electrode was prepared by coating the synthesized material on nickel foam (NF).

For electrode preparation, the nickel foam underwent sequential cleaning with acetone, followed by treatment in 2 M KOH, 1 M HCl, and a final acetone rinse, each for 10, 4, 2, and 5 minutes. Next, a blend of 12 mg of the fabricated material and 2 mg of C was uniformly dispersed in a solvent system composed of -$(C_2H_2F_2)_n$- and C_5H_9NO. The resulting suspension was applied to the nickel foam surface, and the assembled electrode was subsequently dried at elevated temperature. In addition, a non-symmetrical energy storage device was constructed, incorporating the synthesized electrode materials on the positive side, while activated carbon (AC) was employed on the negative side. A layer of cellulose paper functioned as the separator within the cell architecture. To maintain the charge balance, the cathode-to-anode mass ratio (m_+/m_-) was set at 1:2, as determined using Eq. (1) [42].

$$\frac{m_+}{m_-} = \frac{C_-\Delta V_-}{C_+\Delta V_+} \quad (1)$$

In this context, m (g), ΔV (V), and C (F g^{-1}) denote the mass of the material, the voltage range, and the specific capacitance, respectively.

Values for specific capacitance (C_s, F g^{-1}), energy density (ED, Wh kg^{-1}), and power density (PD, W kg^{-1}) were obtained through corresponding formulae presented below [43]:

$$C_s = \frac{I\Delta t}{m\Delta V} \quad (2)$$

$$ED = \frac{1}{2} \times \frac{C_s \Delta V^2 \times 1000}{3600} \quad (3)$$

$$PD = \frac{3600 \times E}{t} \quad (4)$$

Here, m refers to the combined mass of active components in grams, ΔV denotes the voltage range in volts, I is the applied discharge current in amperes, and Δt indicates the duration of discharge in seconds.

3. Results and discussion

To investigate the structural arrangement of the synthesized materials, XRD analysis was utilized, providing insights into their crystalline phases and lattice organization. Fig. 1a illustrates the peaks associated with the ZnCo LDH and ZnCo LDH/CeO_2 structure. For ZnCo LDH (black line) the peaks identified at 2θ values of 12.9, 20.8, 32.4, 33.6, 35.6, 59.4, and 61.7 correspond to the (003), (006), (009), (012), (015), (018), (110), and (113) crystal planes, respectively, in accordance with JCPDS standard 12-0142 [44]. Furthermore, the peaks at 2θ values of 38.8 and 51.9 correspond to $Co(OH)_2$ with crystal planes (102) and (104), consistent with JCPDS standard 51-1731 [45]. The results validate the effective synthesis of ZnCo LDH. The XRD data for the ZnCo LDH/CeO_2

structure (red line) unequivocally indicates integration of ZnCo LDH on CeO_2 nanosheets. Additionally, the deposition of ZnCo LDH on CeO_2 results in the emergence of new peaks in the XRD graph, signifying the incorporation of CeO_2 nanosheets into the structure. JCPDS standard 75-0076 indicates that CeO_2 possesses a simple cubic structure, exhibiting distinctive peaks at 2θ values of 27.9, 33.6, 47.7, 56.5, 59.3, 69.8, and 77.1. The peaks correspond to the (111), (200), (220), (311), (222), (400), and (331) crystallographic planes, respectively [46]. Consequently, the findings validate the effective synthesis of the ZnCo LDH/CeO_2 structure.

Moreover, Fig. 1b displays the XRD data for the CuCo LDH and CuCo LDH/CeO_2 structures. In the case of CuCo LDH (black line) prominent peaks are noted at 2θ values of 12.8 and 25.6, indicating the development of LDH with crystal planes (003) and (006) 199-200 [47,48]. It is worth mentioning that layered double hydroxides often exhibit peaks with 2θ values of 11.7 and 23.2. The displacement of these peaks to elevated angles may be ascribed to the partial deterioration of copper sites [49]. Furthermore, peaks at 2θ values of 20.7 and 38.9 are indicative of $Co(OH)_2$ corresponding to crystal planes (001) and (002) (JCPDS standard 74-1057) [50]. The results validate the effective synthesis of CuCo LDH. Furthermore, as observed in the XRD pattern of the CuCo LDH/CeO_2 structure, the addition of CeO_2 nanosheets introduces new peaks at specific angles, like the ZnCo LDH/CeO_2 structure. These newly formed peaks confirm the successful synthesis and the presence of CeO_2 nanosheets within the CuCo LDH/CeO_2 structure.

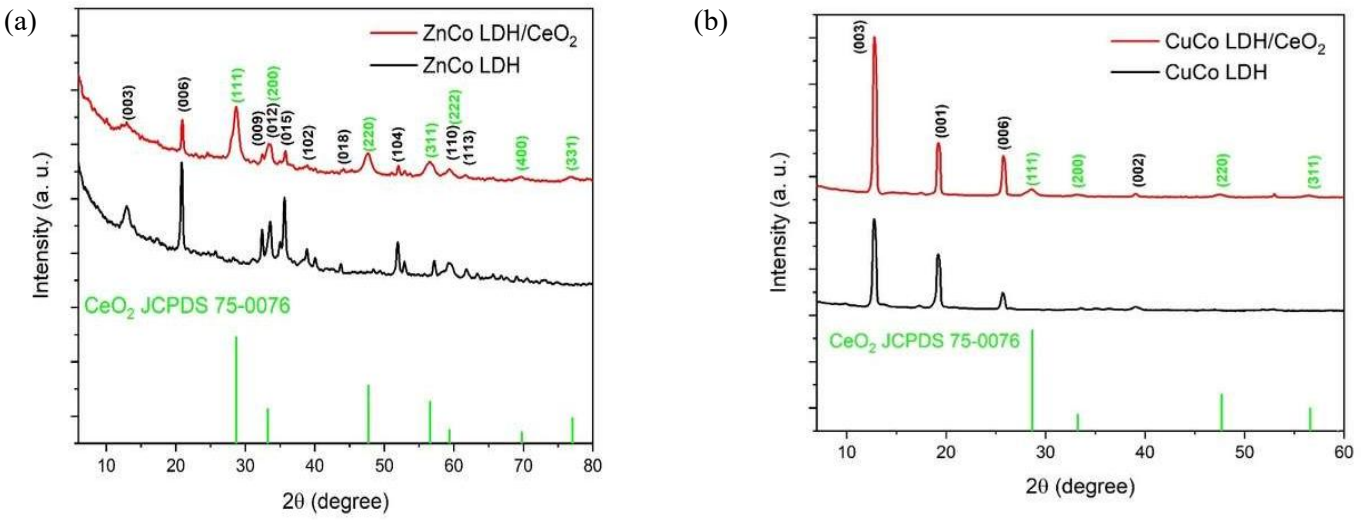

Fig 1. (a) Diffraction profiles of ZnCo LDH and ZnCo LDH/CeO_2; (b) Diffraction profiles of CuCo LDH and CuCo LDH/CeO_2.

Fig. 2a displays the diffraction profiles corresponding to ZnCoS and ZnCoS/CeO_2 structures. As observed in the ZnCoS structure, the crystalline planes (111), (200), (220), (311), (222), (400), and (331) appear at 2θ angles of 28.8, 33.25, 47.7, 56.6, 59.6, 69.7, and 76.9, respectively. The appearance of new peaks indicates structural changes in ZnCo LDH, confirming its transformation into ZnCoS. Notably, this structure follows the JCPDS standard 47-1656 [51]. On the other hand, the XRD pattern of ZnCoS/CeO_2 retains the same crystalline planes as ZnCoS. However, the overlapping diffraction peaks of the sulfide structure with CeO_2 hinder the clear differentiation of their respective peaks.

Furthermore, Fig. 2b displays the XRD patterns of the CuCoS and CuCoS/CeO_2 structures. The data for CuCoS display diffraction peaks at 2θ angles of 26.6, 31.3, 38.0, 46.0, and 54.9, which correspond to the crystalline planes (022), (113), (004), (224), and (044), respectively. The observed peaks validate the fabrication of the $CuCo_2S_4$ structure, according to JCPDS standard 42-1450 [52]. Additionally, the peaks at 27.9, 29.4, 32.0, 32.9, and 48.0 are attributed to CuS,

corresponding to the crystalline planes (101), (102), (103), (006), and (110) based on JCPDS standard 75-2233 [53]. The results validate the effective synthesis of the CuCoS structure. The XRD pattern of $CuCoS/CeO_2$ exhibits additional peaks at 33.3, 47.5, 56.5, 59.4, 69.8, and 77.1, corresponding to the crystalline planes of CeO_2. The results demonstrate that the final composite structure has been effectively formed.

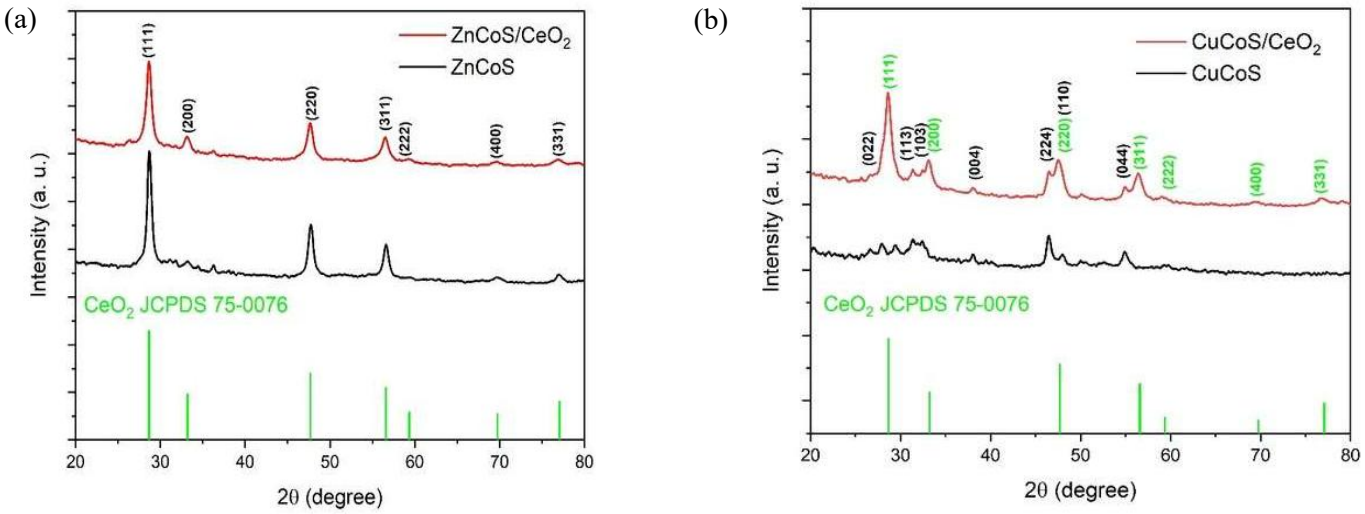

Fig 2. (a) Diffraction profiles of ZnCoS and $ZnCoS/CeO_2$; (b) Diffraction profiles of CuCoS and $CuCoS/CeO_2$.

FESEM was utilized to investigate and visualize the external structural features and surface texture of the fabricated materials. Fig. 3a illustrates the image of CeO_2 nanosheets, characterized by a smooth surface. Fig. 3a is presented at a relatively lower magnification to show the overall sheet-like morphology of the CeO_2 support. Fig. 3b presents the micrograph of the ZnCo LDH structure, which comprises nanorods with a thickness of approximately 200 nm. Following the sulfidation process, the ZnCoS structure is generated. Its micrograph (Fig. 3c) reveals an aggregated particle morphology. Moreover, the micrograph of ZnCo LDH/CeO_2 is depicted in Fig. 3d representation distinctly illustrates the deposition of particles onto CeO_2 nanosheets, so validating the efficacy of

the synthesis method. Following the sulfidation process of ZnCo LDH/CeO_2, the ZnCoS/CeO_2 structure was achieved, as illustrated in Fig. 3e. Sulfidation significantly increases surface porosity, thereby enhancing electrolyte-accessible surface area, exposing more electroactive sites, and facilitating ion/electron transport during charge storage.

The micrograph of the CuCo LDH structure (Fig. 3f) illustrates the development of nanorods with smooth surfaces and consistent particle size and distribution. Furthermore, in Fig. 3g, after the sulfidation treatment, the formerly smooth nanorods exhibit modest porosity. Furthermore, the micrograph of CuCo LDH/CeO_2 (Fig. 3h) reveals the existence of nanoparticles and nanorods affixed to cerium oxide. The detected porosity on the CeO_2 surface enhances electrolyte infiltration. The morphology of CuCoS/CeO_2 (Fig. 3i) closely resembles that of its layered hydroxide precursor, comprising nanorods and nanoparticles with dimensions between 100 and 200 nm. The nanoscale porosity generated during synthesis is anticipated to enhance electrocatalytic performance [54]. In Fig. 3j and 3k, the TEM micrographs of the ZnCoS/CeO_2 and CuCoS/CeO_2 structures are shown, respectively. These images reveal that both structures possess a hollow morphology, which can play a significant role in enhancing their performance by facilitating more efficient electron transport.

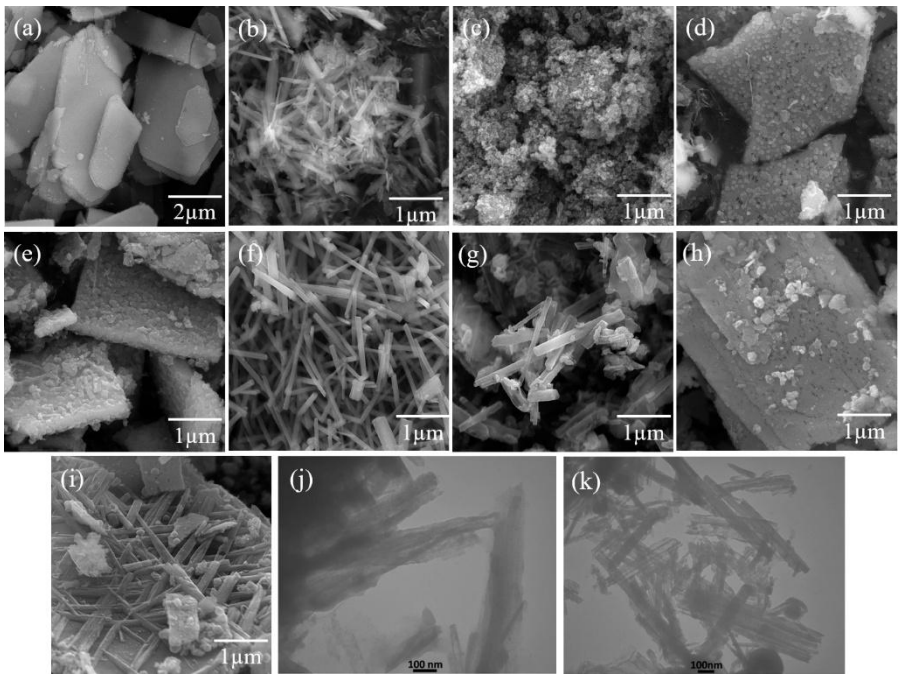

Fig 3. FESEM micrographs of (a) CeO_2, (b) ZnCo LDH, (c) ZnCoS, (d) ZnCo LDH/CeO_2, (e) ZnCoS/CeO_2, (f) CuCo LDH, (g) CuCoS, (h) CuCo LDH/CeO_2, and (i) CuCoS/CeO_2; TEM micrographs of (j) ZnCoS/CeO_2, (k) CuCoS/CeO_2.

Fig. 4a and 4b, illustrate the EDS results and elemental distribution maps for the ZnCoS/CeO_2 sample. The EDS analysis indicates that this structure comprises oxygen, sulfur, zinc, cobalt, and cerium components, hence verifying the effective synthesis of ZnCoS/CeO_2. Moreover, the elemental mapping unequivocally illustrates that all elements are consistently distributed across the surface, signifying the homogenous dispersion of components and corroborating the efficacy of the synthesis process.

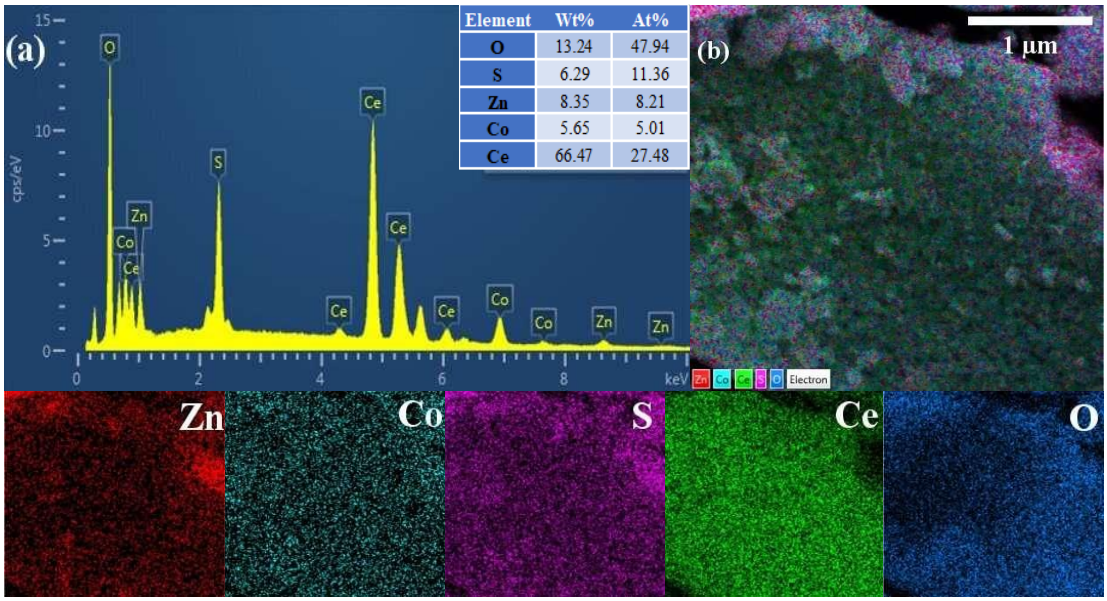

Fig 4. (a) EDS results, and (b) elemental distribution of $ZnCoS/CeO_2$.

The EDS analysis of the $CuCoS/CeO_2$ structure (Fig. 5a) confirms the presence of oxygen, sulfur, cobalt, copper, and cerium elements, validating the effective formation of the intended composition. Moreover, the elemental distribution of this structure (Fig. 5b) demonstrates a uniform distribution of all these elements across the surface [55,56], further validating the homogeneous dispersion and proper synthesis of the $CuCoS/CeO_2$ structure.

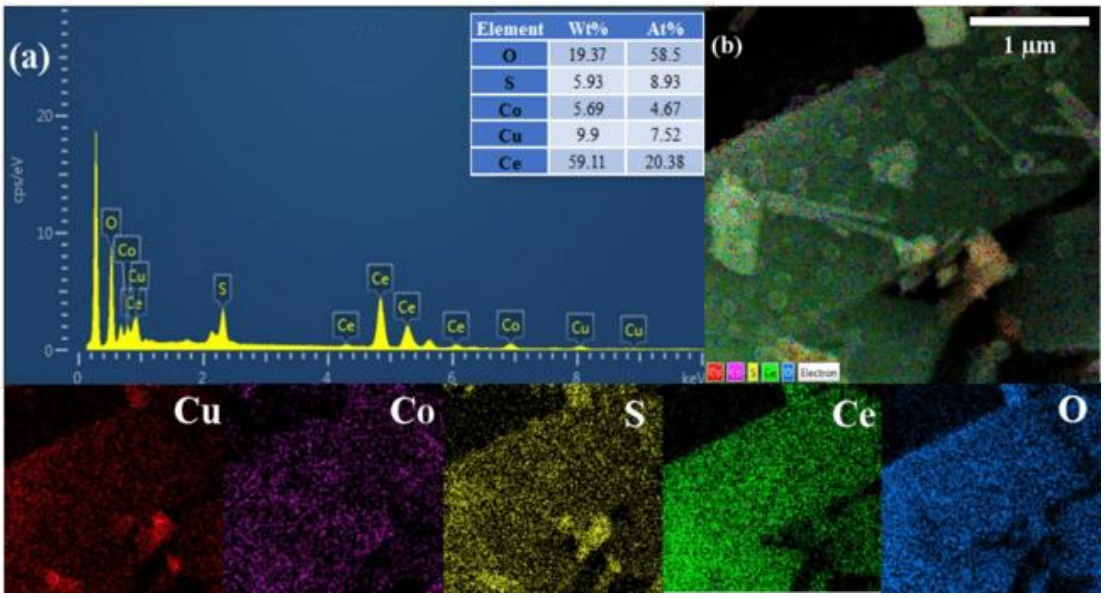

Fig 5. (a) EDS results, and (b) elemental distribution of $CuCoS/CeO_2$.

XPS analysis was carried out to further examine the elemental composition and chemical valence states in $ZnCoS/CeO_2$ (Fig. 6) and $CuCoS/CeO_2$ (Fig. 1S). In the XPS spectrum of the $ZnCoS/CeO_2$ structure, within the binding energy region associated with cobalt (Fig. 6a), deconvoluted peaks at 779.8 and 784.2 eV are assigned to Co $2p_{3/2}$, while those at 795.7 and 800.2 eV correspond to Co $2p_{1/2}$. Furthermore, two satellite peaks were present at 787.3 and 803.5 eV [57,58]. Additionally, based on the results of this analysis, and disregarding the satellite peaks, the amount of Co^{3+} in this structure is 67.18%, and the amount of Co^{2+} is 32.82%. Fig. 6b presents the Ce 3d XPS spectrum. The deconvoluted peaks at binding energies of 880.3, 883.6, 886.8, and 895.9 eV are associated with Ce $3d_{5/2}$, while those observed at 898.8, 904.9, 905.1, and 914.3 eV correspond to Ce $3d_{3/2}$ [59]. Additionally, the measured oxidation-state fractions for Ce^{3+} and Ce^{4+} are 24.88% and 75.12%, respectively. The deconvoluted O 1s spectrum shown in Fig. 6c exhibits three distinct peaks at binding energies of 527.2, 529.4, and 530.6 eV, corresponding to lattice oxygen (O^{2-}), hydroxyl groups (OH^-), and adsorbed water molecules (H_2O), respectively [60]. The S 2p spectrum presented in Fig. 6d displays two primary peaks at 159.4 and 160.6 eV, assigned to S $2p_{3/2}$ and S $2p_{1/2}$, respectively. An additional peak at 166.7 eV suggests the presence of surface-bound sulfur in the form of sulfate species [61]. Fig. 6e illustrates the XPS results for the Zn element. The deconvoluted peaks at 1019.4 eV and 1042.5 eV are attributed to Zn $2p_{3/2}$ and Zn $2p_{1/2}$, respectively; and , Fig. 6f shows Zn LLM peak [62,63].

The XPS analysis of the $CuCoS/CeO_2$ structure is shown in Fig. S1. In Fig. S1a, the deconvoluted peaks associated with Co 2p are evident, with signals at 779.4 eV and 783.8 eV corresponding to Co $2p_{3/2}$, and those at 795.9 eV and 801.3 eV assigned to Co $2p_{1/2}$. Furthermore, two satellite peaks were present at 787.2 and 804.6 eV [58,64]. Moreover, based on the results of this analysis, and

disregarding the satellite peaks, the amount of Co^{3+} in this structure is 65.25%, and the amount of Co^{2+} is 34.75%. The deconvoluted Ce 3d spectrum presented in Fig. S1b shows peaks at binding energies of 880.3, 883.6, 886.7, and 895.9 eV, corresponding to Ce $3d_{5/2}$. In contrast, the peaks at 898.9, 902.1, 905.3, and 914.3 eV are associated with Ce $3d_{3/2}$ [59]. Furthermore, quantification of cerium oxidation states yields 20.97% for Ce^{3+} and 79.03% for Ce^{4+}. The deconvoluted O 1s spectrum (Fig. S1c) displays three distinct peaks: the signal at 527.1 eV is attributed to O^{2-}, the peak at 529.3 eV attributed to OH^-, and the one at 530.6 eV is associated with H_2O [60]. The results corresponding to the S 2p spectrum in Fig. S1d show peaks located at 159.4 eV and 160.8 eV, which are attributed to S $2p_{3/2}$ and S $2p_{1/2}$, respectively. Additionally, similar to the ZnCoS/CeO_2 structure, the peak observed at 166.7 eV indicates the presence of surface sulfur in the form of sulfate [61]. The results related to the Cu 2p spectrum in Fig. S1e confirm the presence of copper metal in the synthesized structure. deconvoluted peaks at 931.7 and 951.8 eV are assigned to Cu $2p_{3/2}$ and Cu $2p_{1/2}$, respectively. While, those at 939.8 and 959.7 eV correspond to satellite peaks; and , Fig. S1f shows Cu LLM peaks [65,66]. It is important to mention that, the coexistence of Ce^{3+} and Ce^{4+} in both composites suggests a defect-associated ceria environment that can support interfacial redox activity and charge-transfer processes [67,68].

Beyond confirming elemental composition, the XPS results provide insight into the electronic structure of the synthesized composites. The coexistence of Co^{2+} and Co^{3+} in both samples indicates the presence of multiple redox-active cobalt centers, which can promote reversible Faradaic reactions and improve pseudocapacitive charge storage behavior. The simultaneous presence of Ce^{3+} and Ce^{4+} further suggests a redox-flexible ceria phase and a defect-rich interfacial environment, both of which are beneficial for charge compensation and electron-transfer processes in composite electrodes [69]. In particular, the slightly higher Ce^{3+} fraction in ZnCoS/CeO_2

compared with $CuCoS/CeO_2$ points to a more reduced ceria environment in the Zn-containing composite, which may contribute to its improved electronic transport and electrochemical activity. The O 1s components assigned to surface hydroxyl species and adsorbed water indicate a hydrated surface chemistry that can facilitate electrolyte penetration and OH^- adsorption during charge storage, although these features should not be used alone as a direct measure of oxygen-vacancy concentration [70,71]. In addition, the S 2p spectra confirm the formation of metal-sulfur bonds, while the high-binding-energy sulfur component is reasonably attributed to superficial oxidized sulfur species formed by partial surface oxidation of sulfides under ambient exposure, a common phenomenon in sulfide-based materials [72]. Therefore, the XPS results support that the superior performance of $ZnCoS/CeO_2$ arises not only from elemental composition but also from a more favorable mixed-valence/defect-assisted electronic environment, which is consistent with its lower resistance and higher capacitance in the electrochemical measurements.

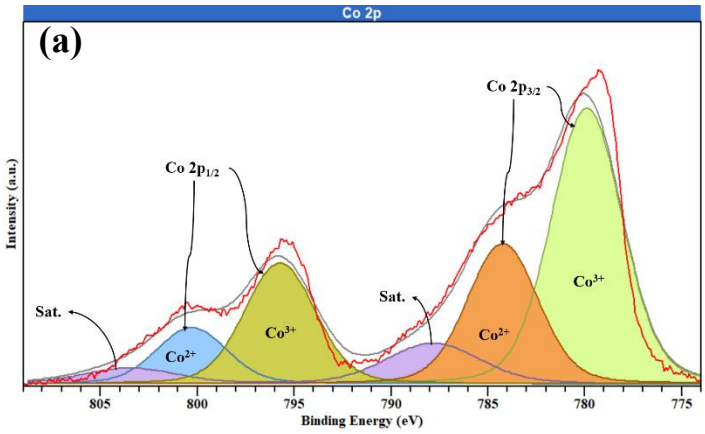

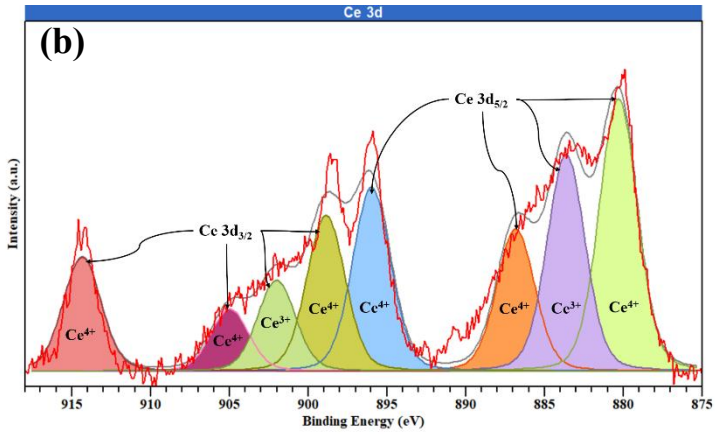

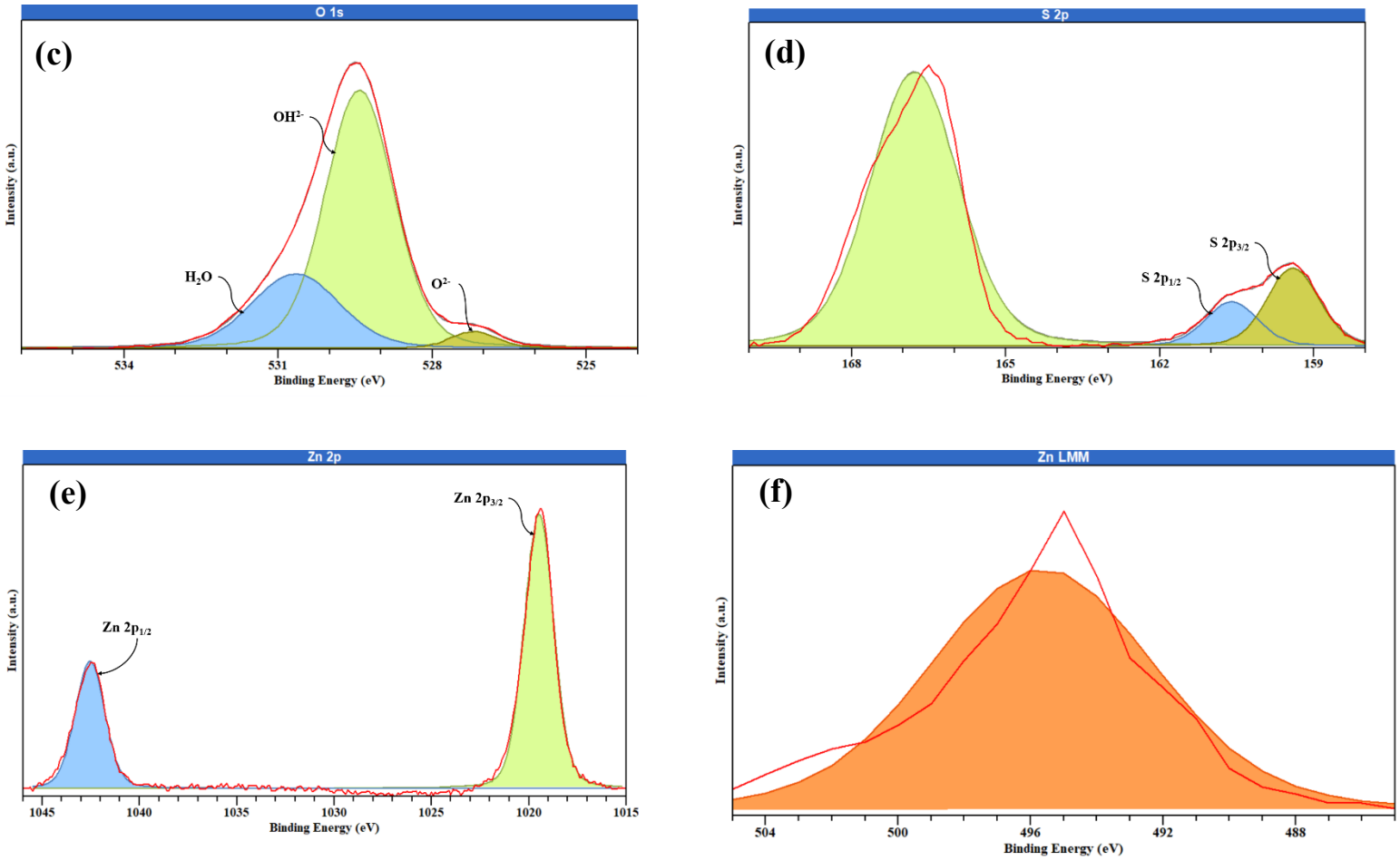

Fig 6. XPS spectrum of (a) Co 2p, (b) Ce 3d, (c) O 1s, (d) S 2p, (e) Zn 2p, and (f) Zn LMM for $ZnCoS/CeO_2$.

A range of electrochemical evaluation methods, namely impedance spectroscopy (EIS), charge-discharge profiling under constant current (GCD), and cyclic voltammetry (CV), was applied using a standard three-electrode setup for detailed performance analysis. For better comparison and clearer visualization of the obtained results, the data for Zn-containing and Cu-containing electrodes are presented in separate graphs. Fig. 7a and Fig. S2a illustrate the CV curves obtained for the synthesized materials measured under a scan rate of 10 mV s^{-1}. It should be noted that these CV curves were recorded in a three-electrode configuration for the positive electrode materials; therefore, the positive and negative current responses in the selected potential window correspond

to the anodic and cathodic branches of the reversible redox process, rather than indicating simultaneous positive-electrode and negative-electrode behavior. Thus, the potential range of -0.2 to 0.4 V vs Ag/AgCl represents the operating window of the redox-active electrode against the reference electrode, while the negative electrode in the assembled asymmetric device is activated carbon, as discussed later in the manuscript. Based on these data, it is obvious that the $ZnCoS/CeO_2$ structure, followed by $CuCoS/CeO_2$, shows the highest capacitance compared to other substances. These results indicate that the use of the bimetallic sulfide structure alongside cerium oxide nanosheets creates a synergistic effect, enhancing electrochemical performance and confirming the effectiveness of the applied synthesis approach. This interpretation is also supported by the XPS results, which reveal mixed Co^{2+}/Co^{3+} and Ce^{3+}/Ce^{4+} states in both composites and a slightly more favorable reduced/defect-associated ceria environment in $ZnCoS/CeO_2$, consistent with its faster charge-transfer behavior. The existence of a pair of redox peaks in the CV curves implies that the electrodes undergo reversible faradaic redox reactions, further validating their battery-type activity [73]. Additionally, within this potential range, the charge transfer process presumably arises from the reactivity of the produced materials with OH^- ions in the electrolyte [74]. The expected reactions for $ZnCoS/CeO_2$ and $CuCoS/CeO_2$ electrodes are described in Eq. (5-7) and Eq. (7-10), respectively [75–77].

$$ZnCo_2S_4+H_2O+OH^- \leftrightarrow ZnSOH+2CoSOH+e^- \quad (5)$$

$$CoSOH+OH^- \leftrightarrow CoSO+ H_2O+e^- \quad (6)$$

$$ZnSOH+OH^- \leftrightarrow ZnSO+ H_2O+ e^- \quad (7)$$

$$CuCo_2S_4+ H_2O+OH^- \leftrightarrow CuSOH+2CoSOH+e^- \quad (8)$$

$$CoSOH+OH^- \leftrightarrow CoSO+ H_2O+e^- \quad (9)$$

$$CuSOH+OH^{-}\leftrightarrow CuSO+ H_2O+e^{-} \quad (10)$$

Further evaluation of the samples' electrochemical performance was performed at constant current densities using the GCD technique. Fig. 7b and Fig. S2b display the GCD profiles, providing additional evidence of the battery-type characteristics exhibited by the synthesized samples. All measurements were made at 1 A g^{-1}. The determined specific capacitances for $ZnCoS/CeO_2$, ZnCo LDH/CeO_2, ZnCoS, ZnCo LDH, $CuCoS/CeO_2$, CuCo LDH/CeO_2, CuCoS, CuCo LDH, and CeO_2 were 616.25, 403, 364, 321.75, 416.25, 351, 335.75, 321.5, and 169 F g^{-1}, respectively. Of them, $ZnCoS/CeO_2$ had the longest discharge duration and the largest specific capacitance, whereas $CuCoS/CeO_2$ also showed a significant specific capacitance. The sulfidation process, along with the incorporation of CeO_2, significantly enhanced the charge storage capabilities of the resulting compounds. This enhancement is attributed to the sulfidation-induced transition from LDH to a more conductive and redox-active sulfide phase together with the formation of a more porous electrode architecture, both of which promote electrolyte access and charge transfer [78–80]. The quantity of oxidation states is essential for attaining elevated capacitance [81]. The lower capacitance observed in copper-based structures compared to those containing manganese can be explained by the narrower range of accessible oxidation states in copper compounds, which restricts their redox activity during charge storage processes.

In Fig. 7c and Fig. S2c, the GCD curves of $ZnCoS/CeO_2$ and $CuCoS/CeO_2$ electrodes are presented at 1, 2, 3, 5, 8, and 10 A g^{-1}. Furthermore, based on the data presented in these figures, capacitance values for the electrodes under varying current conditions were computed and illustrated in Fig. 7d and Fig. S2d. For the $ZnCoS/CeO_2$ sample, the specific capacitance at a power density of 10 A g^{-1} is 40% of its value at 1 A g^{-1}, whereas for the $CuCoS/CeO_2$ sample, this ratio is 30%. These

findings suggest that $CuCoS/CeO_2$ exhibits greater opposition to electron transfer in comparison with $ZnCoS/CeO_2$.

EIS analysis was conducted across a frequency span from 0.1 Hz to 100 kHz to gain deeper insight into electrode behavior. The Nyquist plots for all materials are displayed in Fig. 7e and Fig. S2e. In these plots, the horizontal axis represents overall resistance contributions , including interfacial resistance arising from the junction between the electroactive material and the current collector, inherent resistance within the active substance, ionic resistance from the electrolyte, and barriers to charge transfer [82]. At lower frequencies, the linear segment reflects the impedance related to ion diffusion within the electrode materials. The optimal Nyquist plot of an electrode should manifest as a vertical line in this region; hence, a steeper vertical line within this frequency range indicates superior capacitive performance [83]. The measured solution resistances (R_s) for $ZnCoS/CeO_2$, ZnCo LDH/CeO_2, ZnCoS, ZnCo LDH, $CuCoS/CeO_2$, CuCo LDH/CeO_2, CuCoS, and CuCo LDH were 4.93, 5.12, 5.76, 6.22, 5.43, 5.52, 5.9, and 6.81 Ω, respectively, and are summarized in Table 1. The results indicate that the R_s values of all investigated electrodes are relatively close, suggesting that the ohmic contribution of the electrolyte/electrode system is broadly similar among the samples. Among them, $ZnCoS/CeO_2$ exhibits the lowest R_s value, followed by ZnCo LDH/CeO_2 and $CuCoS/CeO_2$, whereas the precursor LDH electrodes show comparatively higher values. This trend suggests that sulfidation and CeO_2 integration contribute to a modest reduction in the ohmic resistance of the electrode system. However, because the differences in R_s are not large, the superior electrochemical performance of $ZnCoS/CeO_2$ should not be attributed solely to resistance reduction. Rather, its improved behavior is better understood as the result of the combined effect of slightly lower R_s together with more favorable charge-storage characteristics, as evidenced by its higher specific capacitance and better rate capability.

Moreover, the charge transfer resistance (R_{ct}) derived from the Nyquist plots provides important insight into the interfacial faradaic kinetics of the prepared electrodes. As summarized in Table 1, the R_{ct} values vary significantly among the investigated materials, indicating notable differences in electron transfer efficiency at the electrode-electrolyte interface. Among all samples, ZnCoS/CeO_2 exhibits a relatively low R_{ct} value of 1.53 Ω, suggesting that the incorporation of CeO_2 facilitates faster charge transfer and improves the electrochemical activity of the ZnCoS matrix. Similarly, ZnCo LDH/CeO_2 also shows a moderate R_{ct} value of 1.76 Ω, indicating improved electroactive surface accessibility and enhanced redox kinetics due to the synergistic interaction between LDH layers and CeO_2 species. In contrast, pristine materials such as ZnLDH display a significantly higher R_{ct} value (3.01 Ω), reflecting slower interfacial charge transfer and consequently lower capacitance (321.75 F g^{-1}). A similar trend is observed for Cu-based electrodes, where the incorporation of CeO_2 markedly reduces R_{ct}, demonstrating that the heterostructure formation effectively promotes electron transport and accelerates the faradaic reactions. Overall, the reduced R_{ct} values in the composite electrodes clearly indicate improved electrical conductivity and more efficient charge transfer pathways compared with their corresponding pristine counterparts.

In addition to charge transfer resistance, the Warburg impedance (R_w) extracted from the low-frequency region of the Nyquist plots reflects the ion diffusion behavior within the electrode structure. The ZnCoS/CeO_2 electrode shows the lowest R_w value (9.6 Ω), indicating rapid electrolyte ion diffusion and efficient penetration of ions into the active sites of the electrode. This enhanced ion transport is consistent with its outstanding electrochemical performance and suggests that the hybrid structure provides a more accessible porous framework for ion migration. By comparison, the pristine ZnCoS and ZnCo LDH electrodes exhibit higher R_w values of 16.18 and

16.37 Ω, respectively, indicating relatively slower ion diffusion due to the more compact structure and limited ion transport pathways. A similar tendency is observed in the Cu-based systems, where the R_w value decreases from 17.43 Ω in CuCo LDH to 12.71 Ω in CuCo LDH/CeO_2 and 12.01 Ω in CuCoS/CeO_2, confirming that the incorporation of secondary oxide phases significantly improves ion accessibility and electrolyte penetration.

These results collectively demonstrate that the formation of composite or heterostructured electrodes not only reduces the charge transfer resistance but also enhances ion diffusion kinetics, thereby contributing to the improved capacitive performance of the developed supercapacitor materials. Therefore, the EIS results support the conclusion that ZnCoS/CeO_2 provides the most favorable overall electrochemical response among the investigated materials, although the impedance differences are moderate rather than drastic.

Table 1. EIS values of the investigated electrodes obtained from the high-frequency intercept of the Nyquist plots.

Sample	R_s (Ω)	R_{ct} (Ω)	R_w (Ω)
ZnCoS/CeO_2	4.93	1.53	9.6
ZnCo LDH/CeO_2	5.12	1.76	12.82
ZnCoS	5.76	1.87	16.18
ZnCo LDH	6.22	3.01	16.37
CuCoS/CeO_2	5.43	1.79	12.01
CuCo LDH/CeO_2	5.52	1.97	12.71
CuCoS	5.9	2.2	16.35
CuCo LDH	6.81	2.7	17.43

GCD analysis was conducted at 5 A g^{-1} over 2500 cycles to assess the stability of the synthesized structures. The findings for $ZnCoS/CeO_2$ and $CuCoS/CeO_2$ are shown in Fig. 7f and Fig. S2f, respectively. The findings indicate that the specific capacity of both materials experiences a minor rise during the early cycles, attributable to the self-activation of the electrodes [84]. Furthermore, both figures demonstrate a reduction in performance during the cycling process attributable to structural deterioration or trapping of electrolyte ions [85]. Ultimately, the $ZnCoS/CeO_2$ and $CuCoS/CeO_2$ structures preserved 86.7% and 86% of their original capacity after 2500 cycles, respectively, indicating their favorable long-term performance. Coulombic efficiency, defined as the ratio of discharge time to charge time, which reflects the efficiency of charge transfer without loss throughout the charge-discharge process, was determined to be 93.8% for $ZnCoS/CeO_2$ and 94% for $CuCoS/CeO_2$.

The beneficial role of CeO_2 introduction in the present composites is better understood as a heterointerface-assisted synergistic effect rather than a simple addition of a second phase [86,87]. CeO_2 contributes a reversible Ce^{3+}/Ce^{4+} redox couple and a defect-rich ceria surface, and the coexistence of Ce^{3+}/Ce^{4+} is widely associated with oxygen-vacancy-related states that facilitate charge compensation and interfacial ion/electron transport in hybrid electrodes [86,88]. At the same time, the CeO_2 nanosheet framework can act as a dispersive scaffold for the sulfide phase, helping to suppress aggregation, expose more electroactive sites, and shorten electrolyte diffusion pathways [78,87]. In the present work, the beneficial effect of CeO_2 is directly reflected in the electrochemical data: after CeO_2 incorporation, the specific capacitance increases from 364 to 616.25 F g^{-1} for ZnCoS to $ZnCoS/CeO_2$ and from 335.75 to 416.25 F g^{-1} for CuCoS to $CuCoS/CeO_2$. A similar positive effect is also observed for the precursor LDH systems, where the capacitance rises from 321.75 to 403 F g^{-1} for ZnCo LDH to ZnCo LDH/CeO_2 and from 321.5 to

351 F g^{-1} for CuCo LDH to CuCo LDH/CeO_2, confirming that CeO_2 contributes beneficially even before sulfidation. Therefore, in this manuscript, the synergistic effect of CeO_2 introduction should be described as the combined result of redox-active Ce^{3+}/Ce^{4+} chemistry, defect-associated interfacial states, and improved electrolyte accessibility [86].

Moreover, beyond the increase in capacitance, the beneficial role of sulfidation in the present system should be understood as a synergistic phase-and-structure transformation rather than as a simple sulfur substitution step [78,89]. The conversion of the LDH precursor into a bimetallic sulfide phase generally provides a more electrochemically favorable framework, because transition-metal sulfides are widely associated with higher electronic conductivity and richer reversible redox activity than the corresponding hydroxide phases [78,89]. At the same time, sulfidation can preserve useful features of the precursor architecture while generating additional porosity or interparticle voids, which improves electrolyte penetration, shortens ion-diffusion pathways, and increases the exposure of electroactive sites [90,91]. In the present work, this structural contribution is consistent with the FESEM observations, where the sulfidized Zn- and Cu-based samples show more porous features than their corresponding LDH precursors (Fig. 3c-i). The electrochemical data also support the beneficial effect of sulfidation, since the specific capacitance increases from 321.75 to 364 F g^{-1} for ZnCo LDH to ZnCoS and from 403 to 616.25 F g^{-1} for ZnCo LDH/CeO2 to ZnCoS/CeO2, while the Cu-based series follows the same trend, increasing from 321.5 to 335.75 F g^{-1} and from 351 to 416.25 F g^{-1}, respectively (Fig. 7b and Fig. S2b). Therefore, the synergistic effect after sulfidation in this work arises from the combined outcome of a more redox-active sulfide phase, sulfidation-induced porosity, and preserved integration with the CeO_2 nanosheet scaffold, which together improve active-site accessibility and overall electrochemical kinetics [86,89,90].

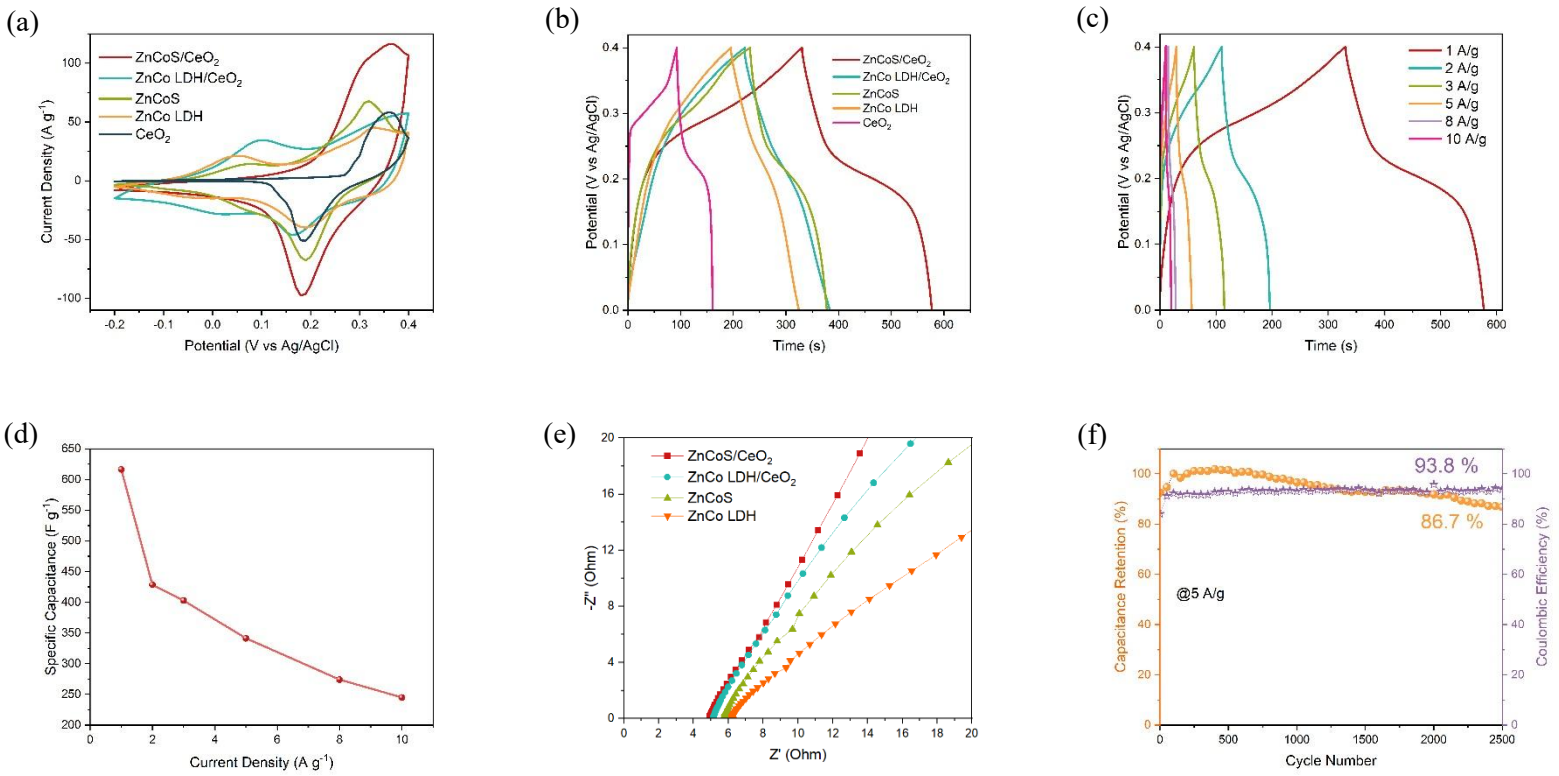

Fig 7. (a) CV analysis of $ZnCoS/CeO_2$, ZnCo LDH/CeO_2, ZnCoS, ZnCo LDH, and CeO_2 at 10 mV s^{-1}; (b) curves of GCD analysis at 1 A g^{-1} for $ZnCoS/CeO_2$, ZnCo LDH/CeO_2, ZnCoS, ZnCo LDH, and CeO_2; (c) GCD curves of $ZnCoS/CeO_2$ at different current densities; (d) Specific capacitance of $ZnCoS/CeO_2$ at different current densities; (e) $ZnCoS/CeO_2$, ZnCo LDH/CeO_2, ZnCoS, and ZnCo LDH Nyquist diagrams; (f) Evaluation of $ZnCoS/CeO_2$ cyclic stability and coulombic efficiency.

Fig. 8 (a,d) presents the CV plots of $ZnCoS/CeO_2$ and $CuCoS/CeO_2$ at multiple scan rates. It is clearly observed that both samples retain the structure of the curves at higher rates, indicating the satisfactory performance of these electrodes. Based on the data from these curves, the logarithmic plot of peak current versus scan rate was constructed using Eq. 11 to estimate the contribution of charge storage processes (Fig. 8 (b,e)) [92].

$$i = a\upsilon^{b} \tag{11}$$

Here, υ represents the scan rate, *i* is the peak current, and *a* and *b* are constants. It is significant that the slope of this plot, represented as *b*, equal to 1, signifies an optimal capacitive-controlled process. Conversely, when the *b*-value approaches 0.5, it suggests that the charge storage mechanism is primarily governed by a diffusion-limited Faradaic reaction. A *b* value situated between these two extremes indicates a hybrid of diffusion-controlled and capacitive-controlled processes. The total involvement of the entire capacity represented as [93]:

$$i(\upsilon) = k_1\upsilon + k_2\upsilon^{1/2} \quad (12)$$

In this equation, the parameter $k_1\upsilon$ represents the capacitive-controlled process, while the parameter $k_2\upsilon^{1/2}$ represents the diffusion-controlled process. For both electrodes, ZnCoS/CeO_2 and CuCoS/CeO_2, at a scan rate of 5 mV s^{-1}, the diffusion-controlled process predominates over the surface-controlled process. With a rise in scan rate, the influence of capacitive control becomes more pronounced, signifying that capacitance-controlled responses prevail in charge storage at elevated rates. At a scan rate of 100 mV s^{-1}, the capacitive contribution peaks at 69% for ZnCoS/CeO_2 and 71% for CuCoS/CeO_2.

A clearer comparison between the Zn-containing and Cu-containing electrodes shows that the difference between the two systems is not limited to absolute capacitance values. ZnCoS/CeO2 delivers a substantially higher specific capacitance than CuCoS/CeO_2 (616.25 versus 416.25 F g^{-1} at 1 A g^{-1}), together with better high-rate retention and lower electrochemical resistance, indicating more favorable charge-transfer kinetics in the Zn-based composite. In addition, the XPS results show slightly higher Co^{3+} and Ce^{3+} fractions for ZnCoS/CeO2 than for CuCoS/CeO2, which suggests a somewhat more favorable mixed-valence surface environment for reversible redox reactions. By contrast, the two electrodes exhibit very similar cycling stability, meaning that the principal distinction between them lies in reaction kinetics and charge-storage efficiency rather

than long-term durability. Therefore, the key finding of this comparative study is that replacing Cu with Zn in the CeO_2-integrated cobalt sulfide framework produces a more electrochemically effective electrode under the present synthesis and testing conditions, and this advantage is maintained at the asymmetric-device level.

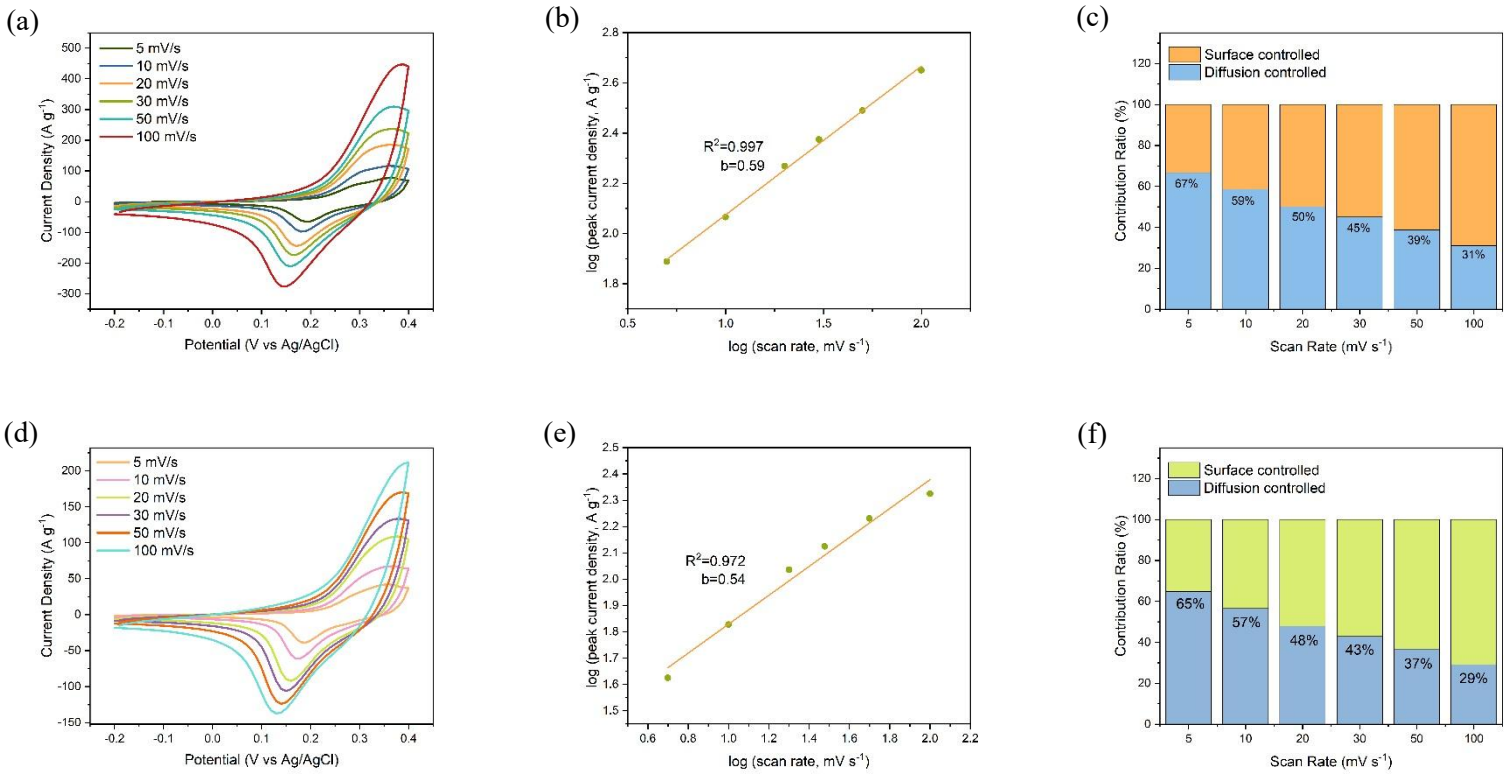

Fig 8. (a) CV diagrams of $ZnCoS/CeO_2$; (b) $ZnCoS/CeO_2$ log (peak current density) vs log (scan rate) curve; (c) the proportion of processes controlled by diffusion to those controlled by capacitive at different scan speeds for $ZnCoS/CeO_2$; (d) CV diagrams of $CuCoS/CeO_2$; (e) $CuCoS/CeO_2$ Log (peak current density) vs log (scan rate) curve; (f) the proportion of processes controlled by diffusion to those controlled by capacitive at different scan speeds for $CuCoS/CeO_2$.

Asymmetric supercapacitors, which consist of two different components for fabricating the cathode and anode, are used for practical electrochemical evaluations. Due to the elevated operating voltage of the cell and the thermodynamic decomposition potential of water, the device's specific capacitance and energy density are both improved by combining the anodic capacitor electrode with the cathodic faradaic electrode. Moreover, asymmetric design enhances the energy density of supercapacitors by using distinct materials for the anode and cathode, facilitating effective energy storage under diverse operating circumstances. Conventionally, an electrostatic double-layer capacitor (EDLC) material functions as the negative electrode, while a Faradaic material operates as the positive electrode. This configuration enhances energy density by increasing the operating cell voltage [94]. Therefore, in this work, $ZnCoS/CeO_2$ and $CuCoS/CeO_2$ structures were used as the cathode, while AC was used as the anode to obtain $ZnCoS/CeO_2$//AC and $CuCoS/CeO_2$//AC. The CV patterns of $ZnCoS/CeO_2$ and $CuCoS/CeO_2$ (Fig. 9(a,b), Fig. S3a) function as a battery-type cathode in the range of -0.2 to 0.4 V. Conversely, the CV curve of AC exhibits EDLC behavior within the range of -1 to 0.

To ascertain the suitable potential window for the supercapacitors, cyclic voltammetry study was conducted at a scan rate of 50 mV s^{-1} across various potential ranges. The findings for $ZnCoS/CeO_2$//AC (Fig. 9c), assessed within the voltage range of 0 to 1.7 V, demonstrate that the curve shape stays consistent up to 1.6 V. The ideal operating voltage for this asymmetric supercapacitor ranges from 0 to 1.6 V. Likewise, the results shown in Fig. S3b indicate that the best potential range for the $CuCoS/CeO_2$//AC structure in this asymmetric supercapacitor ranges from 0 to 1.5 V.

CV analysis was conducted at multiple scan rates for $ZnCoS/CeO_2$//AC and $CuCoS/CeO_2$//AC (Fig. 9d, Fig. S3c). The findings for both electrodes demonstrate that the curve morphologies

remain consistent even at elevated scan speeds, indicating stable redox processes and good reversibility.

Fig. 9e and Fig. S3d show the GCD assessment of the asymmetric supercapacitors at multiple current densities. The findings indicate symmetric configurations with appropriate rate performance for both $ZnCoS/CeO_2$//AC and $CuCoS/CeO_2$//AC asymmetric supercapacitors.

Additionally, based on the GCD measurements, capacitance values for these structures were determined (Fig. 9f, Fig. S3e). The results indicate that $ZnCoS/CeO_2$//AC exhibits better performance compared to $CuCoS/CeO_2$//AC.

In Fig. 9g and Fig. S3f, the Ragone plots of $ZnCoS/CeO_2$//AC and CuCoS/CeO2//AC are presented. For the $ZnCoS/CeO_2$//AC sample, an energy density of 22 Wh kg^{-1} corresponds to a power density of 640 W kg^{-1}, while at an energy density of 11.2 Wh kg^{-1}, the power density reaches 6400 W kg^{-1}. Similarly, for the $CuCoS/CeO_2$//AC sample, the results show that at an energy density of 18.7 Wh kg^{-1}, the asymmetric supercapacitor exhibits a power density of 326 W kg^{-1}, and at an energy density of 8.7 Wh kg^{-1}, the power density is 3260 W kg^{-1}. These results indicate the satisfactory performance of both samples. Furthermore, to better compare the results obtained in this work with those of other works, the performance of the asymmetric supercapacitors shown in the graphs is summarized in Table 2. The comparison indicates that incorporating cerium oxide nanosheets alongside the bimetallic sulfide structure can significantly enhance electron transfer, thereby improving the supercapacitive performance. It can be concluded that the proposed synthesis approach offers a promising strategy for the development of supercapacitors with high-performance.

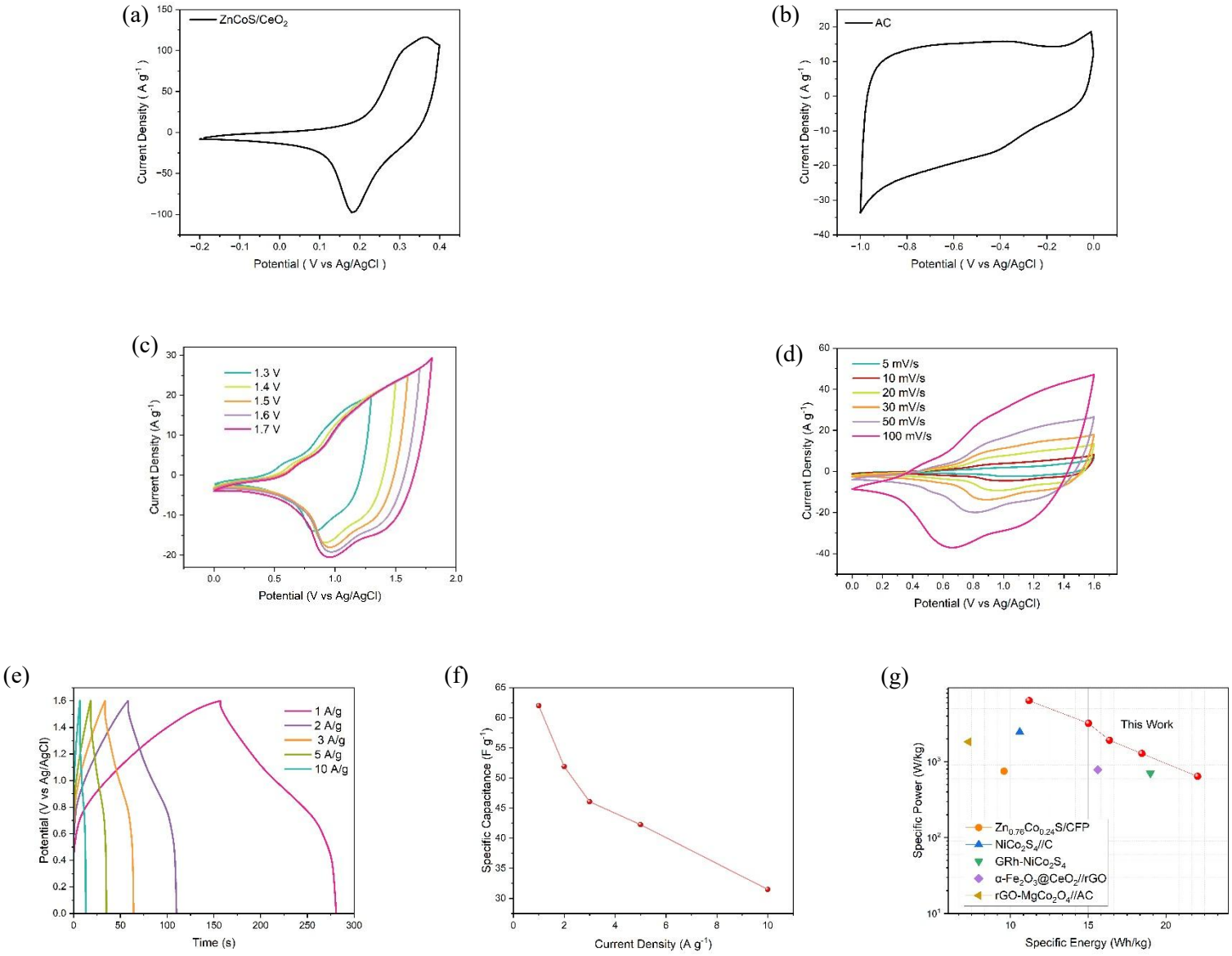

Fig 9. (a) $ZnCoS/CeO_2$ CV diagram; (b) AC CV diagram; (c) $ZnCoS/CeO_2$//AC CV diagrams at different potential windows; (d) CV profiles of $ZnCoS/CeO_2$//AC at different scan rates; (e) GCD diagrams of $ZnCoS/CeO_2$//AC at different current densities; (f) specific capacitances of $ZnCoS/CeO_2$//AC in different current densities; (g) Ragone plot of the $ZnCoS/CeO_2$//AC asymmetric device.

Table 2. The comparison of the results obtained in this work with those of asymmetric supercapacitors reported in other studies.

Name of asymmetric supercapacitor	Result ($Wh\ kg^{-1}$ at $W\ kg^{-1}$)	Reference
$Zn_{0.76}Co_{0.24}S$/Carbon fiber papers//AC	9.59 at 750	[95]
$NiCo_2S_4$//C	10.6 at 2470	[96]
Graphitized rice husk-$NiCo_2S_4$//AC	19 at 703	[97]
α-Fe_2O_3@CeO_2//rGO	15.62 at 781	[98]
rGO-$MgCo_2O_4$//AC	7.3 at 1830	[99]
CoAl-LDH@$Ni(OH)_2$//MWCNT	16.7 at 350	[100]
(CuCo)Se/Nitrogen-doped carbon//AC	16.3 at 155.3	[101]
CoMn LDH//AC	4.4 at 2500	[102]
Cu_2O/CuO/Co_2O_3//Activated graphene	12 at 162	[103]
MnCo Sulfide/ graphene-nickel foam//AC	14.3 at 74.8	[104]
ZnCoS/CeO_2//AC	22 at 640 11.2 at 6400	This work
CuCoS/CeO_2//AC	18.7 at 326 8.7 at 3260	This work

Conclusion

In this study, we introduced a comparative CeO_2-integrated bimetallic sulfide platform based on ZnCoS/CeO_2 and CuCoS/CeO_2 for supercapacitor applications. The main novelty of the work is

the systematic evaluation of how cation selection (Zn versus Cu), together with CeO_2 nanosheet integration and sulfidation, influences the structure and electrochemical response of the resulting electrodes. Among the investigated materials, $ZnCoS/CeO_2$ exhibited the most favorable behavior, demonstrating the highest specific capacitance, and the best asymmetric-device performance. These findings show that CeO_2-assisted structural engineering is effective for both systems, while the Zn-containing composite provides the more advantageous charge-storage configuration in the present study. The enhanced electrochemical behavior of these composites underscores their promise for use in next-generation energy storage technologies like supercapacitors. This work not only provides valuable insights into the design of efficient energy storage systems but also opens new avenues for the development of bimetallic sulfide-based composites for supercapacitor applications.

References

[1] G. Maheshwaran, G. Seethalakshmi, V. Kousalya Devi, L.M. VenkataKrishna, M. Ramesh Prabhu, M. Krishna Kumar, S. Sudhahar, Synergistic effect of Cr2O3 and Co3O4 nanocomposite electrode for high performance supercapacitor applications, Curr. Appl. Phys. 36 (2022) 63–70. https://doi.org/10.1016/j.cap.2022.01.007.

[2] Z. Yousefi, A.A. Asgharinezhad, A. Larimi, C. Ghotbi, Highly efficient electrocatalytic water oxidation based on non-precious metal oxides/sulfides derived from a FeCoNi-metal organic framework, J. Alloys Compd. 1002 (2024) 175214. https://doi.org/10.1016/j.jallcom.2024.175214.

[3] J. Zhang, M. Gu, X. Chen, Supercapacitors for renewable energy applications: A review,

Micro Nano Eng. 21 (2023) 100229. https://doi.org/10.1016/j.mne.2023.100229.

[4] J. Zhang, Energy access challenge and the role of fossil fuels in meeting electricity demand: Promoting renewable energy capacity for sustainable development, Geosci. Front. 15 (2024) 101873. https://doi.org/10.1016/j.gsf.2024.101873.

[5] A.A. Asgharinezhad, A. Bahmani, A. Larimi, F. Khorasheh, C. Ghotbi, Trimetallic (cobalt-nickel-copper) phosphates with cake ball-Like morphology for highly efficient oxygen evolution reaction, J. Alloys Compd. 1024 (2025) 180102. https://doi.org/10.1016/j.jallcom.2025.180102.

[6] S. Maghool, S. Amirnejat, A.A. Nosrati, A.A. Asgharinezhad, A. Larimi, The rise of amorphous water-splitting materials, Coord. Chem. Rev. 560 (2026) 217878. https://doi.org/https://doi.org/10.1016/j.ccr.2026.217878.

[7] S.A. Kadam, R.S. Kate, V.M. Peheliwa, S.A. Shingate, C.C. Sta. Maria, Y.-R. Ma, A comprehensive review on transition metal nitrides electrode materials for supercapacitor: Syntheses, electronic structure engineering, present perspectives and future aspects, J. Energy Storage 72 (2023) 108229. https://doi.org/10.1016/j.est.2023.108229.

[8] L. Zhang, P. Cai, Z. Wei, T. Liu, J. Yu, A.A. Al-Ghamdi, S. Wageh, Synthesis of reduced graphene oxide supported nickel-cobalt-layered double hydroxide nanosheets for supercapacitors, J. Colloid Interface Sci. 588 (2021) 637–645. https://doi.org/10.1016/j.jcis.2020.11.056.

[9] K.A. Sammed, A. Farid, S. Mustafa, A. Kumar, M. Tabish, A.A. Khan, S. Ajmal, Z. Mo, A.R. Akbar, G. Yasin, Y. Zeng, W. Zhao, Developing next-generation supercapacitor electrodes by coordination chemistry-based advanced functional carbon nanostructures:

Progress, Current challenges and prospects, Fuel Process. Technol. 250 (2023) 107896. https://doi.org/10.1016/j.fuproc.2023.107896.

[10] X. Zhang, W. Lu, C. Li, P. Mi, Z. Liu, Y. Li, Y. Tian, X. Ma, F. Liu, X. Jin, Rational design of boron-doped NiCo-glycerate spheres with covered nanosheets for high performance supercapacitors, Mater. Today Chem. 35 (2024) 101826. https://doi.org/10.1016/j.mtchem.2023.101826.

[11] S. Samantaray, D. Mohanty, I.-M. Hung, M. Moniruzzaman, S.K. Satpathy, Unleashing recent electrolyte materials for next-generation supercapacitor applications: A comprehensive review, J. Energy Storage 72 (2023) 108352. https://doi.org/10.1016/j.est.2023.108352.

[12] Z. Yu, E. Liu, K. Xu, X. Yao, J. He, M. Wei, Y. Li, J. Cui, Nanoflower-like heterogeneous NiCo2O4@ NiCoMnS4@NiCo-LDH electrode materials with high-performance supercapacitor, Mater. Today Chem. 46 (2025) 102758. https://doi.org/10.1016/j.mtchem.2025.102758.

[13] M.D. Angelin, S. Rajkumar, A.T. Ravichandran, M.M. Alam, A.G. Al-Sehemi, Optimization of Bi-doped ZnO nanostructures as highly efficient electrode material for symmetric supercapacitor applications, J. Ind. Eng. Chem. 147 (2025) 436–447. https://doi.org/10.1016/j.jiec.2024.12.034.

[14] Y. Yan, L. Zang, T. Dou, H. Li, L. Sun, Y. Zhang, Hollow Co3O4 nanoparticles immobilized rGO/Carbon monolith as an electrode material for high-performance supercapacitors, Ceram. Int. 47 (2021) 20310–20316. https://doi.org/10.1016/j.ceramint.2021.04.039.

[15] B. Kou, Z. Luo, Y. Wang, W. Zhang, L. Chen, Enhancing the performance of wearable fabric-based supercapacitors through functionalized ink interlayer, J. Alloys Compd. 960 (2023) 170809. https://doi.org/10.1016/j.jallcom.2023.170809.

[16] X. Xie, A. Abdukayum, X. Wu, A self-sacrificing template strategy to NiMoSe composites for high-performance supercapacitors, Mater. Today Chem. 47 (2025) 102885. https://doi.org/10.1016/j.mtchem.2025.102885.

[17] R. Govindan, X.-J. Hong, P. Sathishkumar, Y.-P. Cai, F.L. Gu, Construction of metal-organic framework-derived CeO2/C integrated MoS2 hybrid for high-performance asymmetric supercapacitor, Electrochim. Acta 353 (2020) 136502. https://doi.org/10.1016/j.electacta.2020.136502.

[18] B. Liu, Y. Li, S. Qing, K. Wang, J. Xie, Y. Cao, Engineering CuO x –ZrO 2 –CeO 2 nanocatalysts with abundant surface Cu species and oxygen vacancies toward high catalytic performance in CO oxidation and 4-nitrophenol reduction, CrystEngComm 22 (2020) 4005–4013. https://doi.org/10.1039/D0CE00588F.

[19] S. Maghool, A.A. Asgharinezhad, A. Larimi, C. Ghotbi, F. Khorasheh, Enhanced oxygen evolution reaction performance using amorphous hollow cerium-doped cobalt phosphate derived from ZIF-67 structures, J. Alloys Compd. 1008 (2024) 176697. https://doi.org/10.1016/j.jallcom.2024.176697.

[20] M. Karthikeyan, S. Rajkumar, M. Priyadharshan, Green synthesis of Ce doped ZnO nanoparticles using phyllanthus emblica seed extract for the efficient high-performance supercapacitor application, J. Ind. Eng. Chem. 147 (2025) 608–618. https://doi.org/10.1016/j.jiec.2024.12.049.

[21] Z. Wang, K. Zhao, S. Lu, W. Xu, Application of flammulina-velutipes-like CeO2/Co3O4/rGO in high-performance asymmetric supercapacitors, Electrochim. Acta 353 (2020). https://doi.org/10.1016/j.electacta.2020.136599.

[22] D. Majumder, I. Chakraborty, K. Mandal, Room temperature blooming of CeO23D nanoflowers under sonication and catalytic efficacy towards CO conversion, RSC Adv. 10 (2020) 22204–22215. https://doi.org/10.1039/d0ra02554b.

[23] M. Sun, Z. Li, H. Li, Z. Wu, W. Shen, Y.Q. Fu, Mesoporous Zr-doped CeO2 nanostructures as superior supercapacitor electrode with significantly enhanced specific capacity and excellent cycling stability, Electrochim. Acta 331 (2020). https://doi.org/10.1016/j.electacta.2019.135366.

[24] A. Israr, R. Ahmad, K.T. Kubra, Z. Ali, F.J. Iftikhar, G. Ali, Enhanced redox kinetics and capacitance in ceria doped cobalt metal organic framework derived mesoporous carbon electrodes for supercapacitors, J. Ind. Eng. Chem. (2025). https://doi.org/10.1016/j.jiec.2025.06.018.

[25] B. Chameh, N. Khosroshahi, M. Bakhtian, M. Moradi, V. Safarifard, MOF derived CeO2/CoFe2O4 wrapped by pure and oxidized g-C3N4 sheet as efficient supercapacitor electrode and oxygen reduction reaction electrocatalyst materials, Ceram. Int. 48 (2022) 22295–22306. https://doi.org/10.1016/j.ceramint.2022.04.230.

[26] H.T. Das, E.B. T, S. Dutta, N. Das, P. Das, A. Mondal, M. Imran, Recent trend of CeO2-based nanocomposites electrode in supercapacitor: A review on energy storage applications, J. Energy Storage 50 (2022) 104643. https://doi.org/10.1016/j.est.2022.104643.

[27] M. Mazloum-Ardakani, F. Sabaghian, M. Yavari, A. Ebady, N. Sahraie, Enhance the

performance of iron oxide nanoparticles in supercapacitor applications through internal contact of α-Fe2O3@CeO2 core-shell, J. Alloys Compd. 819 (2020). https://doi.org/10.1016/j.jallcom.2019.152949.

[28] X.-M. Cao, J.-Q. Chen, X.-R. Zhao, H. Ge, D. Liu, Q. Wu, Z.-J. Sun, Q. Zhang, Facile synthesis of bead-chain structured MWCNTs@CeO2 with oxygen vacancies-rich for promoting electrochemical energy storage, Chem. Eng. J. 479 (2024) 147663. https://doi.org/10.1016/j.cej.2023.147663.

[29] Z. Liu, C. Pan, W. Li, S. Wei, M. Zhang, S. Chen, A self-template strategy to prepare hollow NiMoS4 nanospheres supported on Ni foam as advanced supercapacitor electrodes, Electrochim. Acta 338 (2020) 135897. https://doi.org/10.1016/j.electacta.2020.135897.

[30] Z. Ji, N. Li, M. Xie, X. Shen, W. Dai, K. Liu, K. Xu, G. Zhu, High-performance hybrid supercapacitor realized by nitrogen-doped carbon dots modified cobalt sulfide and reduced graphene oxide, Electrochim. Acta 334 (2020) 135632. https://doi.org/10.1016/j.electacta.2020.135632.

[31] A. Mohammadi Zardkhoshoui, B. Ameri, S. Saeed Hosseiny Davarani, α-MnS@Co3S4 hollow nanospheres assembled from nanosheets for hybrid supercapacitors, Chem. Eng. J. 422 (2021) 129953. https://doi.org/10.1016/j.cej.2021.129953.

[32] M.S. Mohamed Saleem, R. Swaminathan, V. Mohan, N.U.H. Liyakath Ali, S.-J. Kim, Sulfurization of cobalt oxide to cobalt sulfide: A positrode for the high-performance supercapacitor, J. Ind. Eng. Chem. 136 (2024) 493–500. https://doi.org/10.1016/j.jiec.2024.02.038.

[33] S.S. Rabbani, H. Mustafa, A. Zafar, S. Javaid, M.A. Bakar, A. Nisar, Y. Liu, S. Karim, H.

Sun, S. Hussain, Z. Zafar, Y. Faiz, F. Faiz, Y. Yu, M. Ahmad, Nickel foam supported hierarchical NiCo2S4@NiFe LDH heterostructures as highly efficient electrode for long cycling stability supercapacitor, Electrochim. Acta 446 (2023) 142098. https://doi.org/10.1016/j.electacta.2023.142098.

[34] Z. Sheng, X. Lin, Y. Zhao, X. Zhu, Y. Zhang, L. Huang, D. Xu, Y. Wang, Three-dimensional hierarchical carbon-incorporated Ni3S2@Mn–Co–S@Co9S8 composite on Ni foam for high-performance hybrid supercapacitors, Ceram. Int. 48 (2022) 26660–26668. https://doi.org/10.1016/j.ceramint.2022.05.360.

[35] Z. Bairami, A.A. Asgharinezhad, J.M. Courtney, A. Larimi, F. Khorasheh, A novel CoCuNi-sulfide nanocatalyst derived from trimetallic zeolitic imidazolate framework for boosting oxygen evolution reaction performance: Comparison study of sulfides and oxides, Mater. Today Chem. 42 (2024) 102398. https://doi.org/10.1016/j.mtchem.2024.102398.

[36] X. Zhao, Q. Bi, C. Yang, K. Tao, L. Han, Design of trimetallic sulfide hollow nanocages from metal–organic frameworks as electrode materials for supercapacitors, Dalt. Trans. 50 (2021) 15260–15266. https://doi.org/10.1039/D1DT02819G.

[37] S. Jia, J. Wei, B. Gong, J. Wei, Z. Shao, Sulfur vacancies enriched Nickel-Cobalt sulfides hollow spheres with high performance for All-Solid-State hybrid supercapacitor, J. Colloid Interface Sci. 601 (2021) 640–649. https://doi.org/10.1016/j.jcis.2021.05.127.

[38] B.A. Mola, G. Mani, S. Sambasivam, M.R. Pallavolu, A.A. Ghfar, M. Ouladsmane, M. Alsawat, N.R. Reddy, Y. Noh, S.K. Jilcha, H.-J. Kim, I.M. Obaidat, Y.A. Kumar, Crafting nanoflower-built MnCo2S4 anchored to Ni foam as a prominent energy conversion and energy storage electrode for high-performance supercapacitor applications, J. Energy

Storage 43 (2021) 103155. https://doi.org/10.1016/j.est.2021.103155.

[39] N. Jabeen, A. Hussain, Z. Ullah, T. ul Haq, E.R. Elsharkawy, Z.M. El-Bahy, M.M. Hessien, Design and performance evaluation of hierarchical ZnCo2S4@PANI core-shell nanorod arrays for high-efficiency supercapacitor applications, Mater. Chem. Phys. 320 (2024). https://doi.org/10.1016/j.matchemphys.2024.129462.

[40] Z. Yang, Y. Chen, Q. Tian, H. Zhang, Y. Hou, J. Guo, CuCo2S4@MnO2 hollow porous heterostructure for high-performance supercapacitors, J. Alloys Compd. 989 (2024) 174361. https://doi.org/10.1016/j.jallcom.2024.174361.

[41] A. Mohammadi Zardkhoshoui, R. Arian, S.S. Hosseiny Davarani, Tunable construction of CuS nanosheets@flower-like ZnCo-layered double hydroxide nanostructures for hybrid supercapacitors, Ind. Chem. Mater. 1 (2023) 443–457. https://doi.org/10.1039/D3IM00027C.

[42] C.V.V.M. Gopi, R. Vinodh, S. Sambasivam, I.M. Obaidat, S. Singh, H.-J. Kim, Co9S8-Ni3S2/CuMn2O4-NiMn2O4 and MnFe2O4-ZnFe2O4/graphene as binder-free cathode and anode materials for high energy density supercapacitors, Chem. Eng. J. 381 (2020) 122640. https://doi.org/10.1016/j.cej.2019.122640.

[43] J. Zheng, X. Pan, X. Huang, D. Xiong, Y. Shang, X. Li, N. Wang, W.-M. Lau, H.Y. Yang, Integrated NiCo2-LDHs@MXene/rGO aerogel: Componential and structural engineering towards enhanced performance stability of hybrid supercapacitor, Chem. Eng. J. 396 (2020) 125197. https://doi.org/10.1016/j.cej.2020.125197.

[44] X. Zou, A. Goswami, T. Asefa, Efficient Noble Metal-Free (Electro)Catalysis of Water and Alcohol Oxidations by Zinc–Cobalt Layered Double Hydroxide, J. Am. Chem. Soc. 135

(2013) 17242–17245. https://doi.org/10.1021/ja407174u.

[45] C. Wang, Z. Liu, Y. Sun, X. Liu, Y. Wang, J. Liu, Honeycomb-like MgCo2O4@ZnCo layered double hydroxide as novel electrode material for high-performance all-solid-state supercapacitors, Appl. Surf. Sci. 612 (2023) 155661. https://doi.org/https://doi.org/10.1016/j.apsusc.2022.155661.

[46] D. Maheta, B. Madhukar, A. Tanna, Solution combustion synthesis for rare earth nano metal oxides using D-glycine as fuel: morphological and optical studies, Phys. Scr. 99 (2024). https://doi.org/10.1088/1402-4896/ad9099.

[47] I. Said, M.R. Abukhadra, A.M. Rabie, A.-S.A. Bakr, J.-J. Shim, S.A. Ahmed, Facile Fabrication of ZnMgAl/LDH/Algae Composites as a Potential Adsorbent for Cr(VI) Ions from Water: Fabrication and Equilibrium Studies, ACS Omega 5 (2020) 31342–31351. https://doi.org/10.1021/acsomega.0c04842.

[48] A. Cao, G. Liu, L. Wang, J. Liu, Y. Yue, L. Zhang, Y. Liu, Growing layered double hydroxides on CNTs and their catalytic performance for higher alcohol synthesis from syngas, J. Mater. Sci. 51 (2016) 5216–5231. https://doi.org/10.1007/s10853-016-9823-9.

[49] H. Liu, Q. Jiao, Y. Zhao, H. Li, C. Sun, X. Li, Mixed oxides derived from Cu–Co layered double hydroxide nanorods: Preparation, characterization and their catalytic activities, J. Alloys Compd. 496 (2010) 317–323. https://doi.org/10.1016/j.jallcom.2010.02.004.

[50] B. Liu, T. Xiao, X. Sun, H.-Q. Peng, X. Wang, Y. Zhao, W. Zhang, Y.-F. Song, Hierarchical trace copper incorporation activated cobalt layered double hydroxide as a highly selective methanol conversion electrocatalyst to realize energy-matched photovoltaic-electrocatalytic formate and hydrogen co-production, J. Mater. Chem. A 10 (2022) 19649–19661.

https://doi.org/10.1039/D2TA01104B.

[51] A. Karimi, A.A. Ensafi, B. Rezaei, Design and fabrication of MOF-derived leaf-like Zn-Co-S nanosheet arrays decorated with Ni-Zn-P ultrathin nanostructure for hybrid supercapacitors, Fuel 334 (2023) 126536. https://doi.org/10.1016/j.fuel.2022.126536.

[52] A.T.A. Ahmed, S.M. Pawar, A.I. Inamdar, H. Im, H. Kim, Fabrication of FeO@CuCo 2 S 4 multifunctional electrode for ultrahigh-capacity supercapacitors and efficient oxygen evolution reaction, Int. J. Energy Res. 44 (2020) 1798–1811. https://doi.org/10.1002/er.5027.

[53] T. Li, Z. Zhao, Z. Su, R. Sun, X. Li, Y. Shang, CuCoNi–S anchored CoMoO 4 /MoO 3 forming core–shell structure for high-performance asymmetric supercapacitors, Dalt. Trans. 51 (2022) 16111–16118. https://doi.org/10.1039/D2DT02532A.

[54] S. Maghool, A.A. Asgharinezhad, A. Larimi, C. Ghotbi, F. Khorasheh, Efficient electrocatalysts for OER: Amorphous cerium-doped cobalt sulfide with enhanced performance and durability, Surfaces and Interfaces 54 (2024) 105108. https://doi.org/10.1016/j.surfin.2024.105108.

[55] A.A. Asgharinezhad, H. Ebrahimzadeh, A novel polymer coated magnetic porous carbon nanocomposite derived from a metal-organic framework for multi-target environmental pollutants preconcentration, J. Chromatogr. A 1634 (2020) 461664. https://doi.org/10.1016/j.chroma.2020.461664.

[56] A.A. Asgharinezhad, H. Ebrahimzadeh, Magnetic porous carbon nanocomposite derived from cobalt based-metal-organic framework for extraction and determination of homo and hetero-polycyclic aromatic hydrocarbons, Talanta 233 (2021) 122526.

https://doi.org/10.1016/j.talanta.2021.122526.

[57] J. Li, Z. Li, F. Ning, L. Zhou, R. Zhang, M. Shao, M. Wei, Ultrathin Mesoporous Co 3 O 4 Nanosheet Arrays for High-Performance Lithium-Ion Batteries, ACS Omega 3 (2018) 1675–1683. https://doi.org/10.1021/acsomega.7b01832.

[58] T. Ioannides, M. Smyrnioti, Synthesis of Cobalt-Based Nanomaterials from Organic Precursors, in: M. Khan (Ed.), IntechOpen, London, 2017. https://doi.org/10.5772/intechopen.70947.

[59] N. Fifere, A. Airinei, M. Dobromir, L. Sacarescu, S.I. Dunca, Revealing the Effect of Synthesis Conditions on the Structural, Optical, and Antibacterial Properties of Cerium Oxide Nanoparticles, Nanomaterials 11 (2021) 2596. https://doi.org/10.3390/nano11102596.

[60] L.Q. Guo, S.X. Qin, B.J. Yang, D. Liang, L.J. Qiao, Effect of hydrogen on semiconductive properties of passive film on ferrite and austenite phases in a duplex stainless steel, Sci. Rep. 7 (2017) 3317. https://doi.org/10.1038/s41598-017-03480-8.

[61] S.A. Ansari, H.M. Kotb, M.M. Ahmad, Wrinkle-Shaped Nickel Sulfide Grown on Three-Dimensional Nickel Foam: A Binder-Free Electrode Designed for High-Performance Electrochemical Supercapacitor Applications, Crystals 12 (2022) 757. https://doi.org/10.3390/cryst12060757.

[62] N.T. Mai, T.T. Thuy, D.M. Mott, S. Maenosono, Chemical synthesis of blue-emitting metallic zinc nano-hexagons, CrystEngComm 15 (2013) 6606. https://doi.org/10.1039/c3ce40801a.

[63] G.K. V S, M. M G, XPS analysis of ZnS0.4Se0.6 thin films deposited by spray pyrolysis technique, J. Electron Spectros. Relat. Phenomena 249 (2021) 147072. https://doi.org/10.1016/j.elspec.2021.147072.

[64] X. Zhu, S. Xie, X. Fu, S. Zhu, Y. Min, Q. Xu, Q. Li, High-dispersion Co/N/C ultra-thin carbon nanosheets modified with trace Ce as efficient oxygen reduction reaction catalysts, New J. Chem. 47 (2023) 9153–9163. https://doi.org/10.1039/D3NJ00108C.

[65] F. Peng, Y. Sun, Y. Lu, W. Yu, M. Ge, J. Shi, R. Cong, J. Hao, N. Dai, Studies on Sensing Properties and Mechanism of CuO Nanoparticles to H2S Gas, Nanomaterials 10 (2020) 774. https://doi.org/10.3390/nano10040774.

[66] A.C. Poulose, S. Veeranarayanan, M.S. Mohamed, R.R. Aburto, T. Mitcham, R.R. Bouchard, P.M. Ajayan, Y. Sakamoto, T. Maekawa, D.S. Kumar, Multifunctional Cu2−xTe Nanocubes Mediated Combination Therapy for Multi-Drug Resistant MDA MB 453, Sci. Rep. 6 (2016) 35961. https://doi.org/10.1038/srep35961.

[67] S. Sharma, P. Chand, Supercapacitor and electrochemical techniques: A brief review, Results Chem. 5 (2023) 100885. https://doi.org/https://doi.org/10.1016/j.rechem.2023.100885.

[68] Z.-K. Han, W. Liu, Y. Gao, Advancing the Understanding of Oxygen Vacancies in Ceria: Insights into Their Formation, Behavior, and Catalytic Roles, JACS Au 5 (2025) 1549–1569. https://doi.org/10.1021/jacsau.5c00095.

[69] S.L. Swartz, Catalysis by Ceria and Related Materials Edited by Alessandro Trovarelli (Università di Udine, Italy). Catalytic Science Series. Volume 2. Series Edited by Graham J. Hutchings. Imperial College Press: London. 2002. vviii + 508 pp. $78.00. ISBN: 1-

86094-299-7., J. Am. Chem. Soc. 124 (2002) 12923–12924. https://doi.org/10.1021/ja025256e.

[70] C.D. Easton, D.J. Morgan, Critical examination of the use of x-ray photoelectron spectroscopy (XPS) O 1s to characterize oxygen vacancies in catalytic materials and beyond, J. Vac. Sci. Technol. A 43 (2025) 53205. https://doi.org/10.1116/6.0004686.

[71] Z. Wu, L. Huang, H. Liu, M. Li, H. Wang, Surface oxidation of transition metal sulfide and phosphide nanomaterials, Nano Res. 14 (2021) 2264–2267. https://doi.org/10.1007/s12274-020-3219-5.

[72] M. Fantauzzi, B. Elsener, D. Atzei, A. Rigoldi, A. Rossi, Exploiting XPS for the identification of sulfides and polysulfides, RSC Adv. 5 (2015) 75953–75963. https://doi.org/10.1039/C5RA14915K.

[73] Z. Molaei, A.A. Asgharinezhad, A. Larimi, C. Ghotbi, F. Khorasheh, Incorporation of CeO 2 Nanosheets into MnCoSx Hollow Nanorods for Next Generation Supercapacitors, Energy & Fuels (2025). https://doi.org/10.1021/acs.energyfuels.4c05048.

[74] E. Niknam, H. Naffakh-Moosavy, S.E. Moosavifard, M. Ghahraman Afshar, Amorphous V-doped Co3S4 yolk-shell hollow spheres derived from metal-organic framework for high-performance asymmetric supercapacitors, J. Alloys Compd. 895 (2022) 162720. https://doi.org/10.1016/j.jallcom.2021.162720.

[75] T.-F. Yi, H. Chang, T.-T. Wei, S.-Y. Qi, Y. Li, Y.-R. Zhu, Approaching high-performance electrode materials of ZnCo2S4 nanoparticle wrapped carbon nanotubes for supercapacitors, J. Mater. 7 (2021) 563–576. https://doi.org/10.1016/j.jmat.2020.11.015.

[76] L. Kang, C. Huang, J. Zhang, M. Zhang, N. Zhang, S. Liu, Y. Ye, C. Luo, Z. Gong, C. Wang, X. Zhou, X. Wu, S.C. Jun, Effect of fluorine doping and sulfur vacancies of CuCo2S4 on its electrochemical performance in supercapacitors, Chem. Eng. J. 390 (2020) 124643. https://doi.org/10.1016/j.cej.2020.124643.

[77] Y. Wang, X. Huang, X. Yu, X. Chen, J. Jiang, S. Han, Sponge-like 3D flower-like core-shell heterostructure CuCo2O4@CuCo2S4 as advanced electrodes for high-performance supercapacitor, J. Power Sources 551 (2022) 232186. https://doi.org/10.1016/j.jpowsour.2022.232186.

[78] M. Shariq, D. Alhashmialameer, H. Adawi, M.R. Alrahili, M.Y.A. Almashnowi, A. Alzahrani, M. Sharma, S.K. Ali, Y. Slimani, Advancements in transition metal sulfide supercapacitors: A focused review on high-performance energy storage, J. Ind. Eng. Chem. 144 (2025) 269–291. https://doi.org/https://doi.org/10.1016/j.jiec.2024.11.012.

[79] J. Yan, J. Lu, Y. Sheng, Y. Sun, D. Zhang, Research Progress in the Preparation of Transition Metal Sulfide Materials and Their Supercapacitor Performance, Micromachines 15 (2024) 849. https://doi.org/10.3390/mi15070849.

[80] Y. Gao, L. Zhao, Review on recent advances in nanostructured transition-metal-sulfide-based electrode materials for cathode materials of asymmetric supercapacitors, Chem. Eng. J. 430 (2022) 132745. https://doi.org/https://doi.org/10.1016/j.cej.2021.132745.

[81] A.J.C. Mary, C.I. Sathish, A. Vinu, A.C. Bose, Electrochemical Performance of rGO/NiCo 2 O 4 @ZnCo 2 O 4 Ternary Composite Material and the Fabrication of an all-Solid-State Supercapacitor Device, Energy & Fuels 34 (2020) 10131–10141. https://doi.org/10.1021/acs.energyfuels.0c01427.

[82] A.N. Naveen, S. Selladurai, Investigation on physiochemical properties of Mn substituted spinel cobalt oxide for supercapacitor applications, Electrochim. Acta 125 (2014) 404–414. https://doi.org/10.1016/j.electacta.2014.01.161.

[83] N.O. Laschuk, E.B. Easton, O. V. Zenkina, Reducing the resistance for the use of electrochemical impedance spectroscopy analysis in materials chemistry, RSC Adv. 11 (2021) 27925–27936. https://doi.org/10.1039/D1RA03785D.

[84] R.R. Salunkhe, K. Jang, H. Yu, S. Yu, T. Ganesh, S.-H. Han, H. Ahn, Chemical synthesis and electrochemical analysis of nickel cobaltite nanostructures for supercapacitor applications, J. Alloys Compd. 509 (2011) 6677–6682. https://doi.org/10.1016/j.jallcom.2011.03.136.

[85] E. Mahmud, M.R. Islam, Improved electrochemical performance of bio-derived plasticized starch/ reduced graphene oxide/ molybdenum disulfide ternary nanocomposite for flexible energy storage applications, Sci. Rep. 13 (2023) 20967. https://doi.org/10.1038/s41598-023-48326-8.

[86] R. Govindan, G.S. Lekshmi, R. Ramesh, S. Shanavas, M. Abu Haija, F.L. Gu, Ceria and ceria-based hybrid nanostructures as potential electrode materials for high-performance electrochemical supercapacitors, Mater. Today Chem. 34 (2023) 101779. https://doi.org/https://doi.org/10.1016/j.mtchem.2023.101779.

[87] X. Hu, K. Tao, L. Han, CeO2 decorated on Co-ZIF-L-derived nickel–cobalt sulfide hollow nanosheet arrays for high-performance supercapacitors, Dalt. Trans. 51 (2022) 16093–16101. https://doi.org/10.1039/D2DT02300H.

[88] A. Othman, A. Gowda, D. Andreescu, M.H. Hassan, S. V Babu, J. Seo, S. Andreescu, Two

decades of ceria nanoparticle research: structure, properties and emerging applications, Mater. Horizons 11 (2024) 3213–3266. https://doi.org/10.1039/D4MH00055B.

[89] M. Zhu, D. Wang, Z. Ge, L. Pan, Y. Chen, W. Wang, N. Mitsuzaki, S. Jia, Z. Chen, Recent advances in transition metal sulfide-based electrode materials for supercapacitors, Chem. Commun. 61 (2025) 8314–8326. https://doi.org/10.1039/D5CC01411E.

[90] F. Ran, M. Hu, S. Deng, K. Wang, W. Sun, H. Peng, J. Liu, Designing transition metal-based porous architectures for supercapacitor electrodes: a review, RSC Adv. 14 (2024) 11482–11512. https://doi.org/10.1039/D4RA01320D.

[91] Y.-W. Long, H.-Y. Zeng, H.-B. Li, K.-M. Zou, S. Xu, X.-J. Cao, Sulfidation of CoAl-layered double hydroxide on Ni foam for high-performance supercapacitors, Electrochim. Acta 361 (2020) 137098. https://doi.org/https://doi.org/10.1016/j.electacta.2020.137098.

[92] S. Pang, L. Gong, N. Du, H. Luo, K. Yu, J. Gao, Z. Zheng, B. Zhou, Formation of high-performance Cu-WOx@C tribasic composite electrode for aqueous symmetric supercapacitor, Mater. Today Energy 13 (2019) 239–248. https://doi.org/10.1016/j.mtener.2019.05.016.

[93] M. Alzaid, F. Alsalh, M.Z. Iqbal, Biomass derived activated carbon based hybrid supercapacitors, J. Energy Storage 40 (2021) 102751. https://doi.org/10.1016/j.est.2021.102751.

[94] E. Niknam, H. Naffakh-Moosavy, S.E. Moosavifard, M.G. Afshar, Multi-shelled bimetal V-doped Co3O4 hollow spheres derived from metal organic framework for high performance supercapacitors, J. Energy Storage 44 (2021) 103508. https://doi.org/10.1016/j.est.2021.103508.

[95] M. Zhang, Y. Sui, X. Yuan, J. Qi, F. Wei, Q. Meng, Y. He, Y. Ren, Z. Sun, J. Liu, Controllable Zn0.76Co0.24S Nanoflower Arrays Grown on Carbon Fiber Papers for High-Performance Supercapacitors, Nano 14 (2019) 1950030. https://doi.org/10.1142/S1793292019500309.

[96] W. Kong, C. Lu, W. Zhang, J. Pu, Z. Wang, Homogeneous core–shell NiCo 2 S 4 nanostructures supported on nickel foam for supercapacitors, J. Mater. Chem. A 3 (2015) 12452–12460. https://doi.org/10.1039/C5TA02432C.

[97] Y. Li, F. An, H. Wu, S. Zhu, C. Lin, M. Xia, K. Xue, D. Zhang, K. Lian, A NiCo2S4 /hierarchical porous carbon for high performance asymmetrical supercapacitor, J. Power Sources 427 (2019) 138–144. https://doi.org/10.1016/j.jpowsour.2019.04.060.

[98] M. Mazloum-Ardakani, F. Sabaghian, M. Yavari, A. Ebady, N. Sahraie, Enhance the performance of iron oxide nanoparticles in supercapacitor applications through internal contact of α-Fe2O3@CeO2 core-shell, J. Alloys Compd. 819 (2020) 152949. https://doi.org/10.1016/j.jallcom.2019.152949.

[99] S.G. Krishnan, M. Harilal, B. Pal, I.I. Misnon, C. Karuppiah, C.-C. Yang, R. Jose, Improving the symmetry of asymmetric supercapacitors using battery-type positive electrodes and activated carbon negative electrodes by mass and charge balance, J. Electroanal. Chem. 805 (2017) 126–132. https://doi.org/10.1016/j.jelechem.2017.10.029.

[100] H. Li, F. Musharavati, J. Sun, F. Jaber, E. Zalnezhad, K.N. Hui, K.S. Hui, Investigation of the Electrochemical Properties of CoAl-Layered Double Hydroxide/Ni(OH) 2, J. Electrochem. Soc. 165 (2018) A407–A415. https://doi.org/10.1149/2.0111803jes.

[101] P. Sun, J. Zhang, J. Huang, L. Wang, P. Wang, C. Cai, M. Lu, Z. Yao, Y. Yang, Bimetallic

MOF-derived (CuCo)Se nanoparticles embedded in nitrogen-doped carbon framework with boosted electrochemical performance for hybrid supercapacitor, Mater. Res. Bull. 137 (2021) 111196. https://doi.org/10.1016/j.materresbull.2020.111196.

[102] A.D. Jagadale, G. Guan, X. Li, X. Du, X. Ma, X. Hao, A. Abudula, Ultrathin nanoflakes of cobalt–manganese layered double hydroxide with high reversibility for asymmetric supercapacitor, J. Power Sources 306 (2016) 526–534. https://doi.org/10.1016/j.jpowsour.2015.12.097.

[103] M. Kuang, T. Tao Li, H. Chen, S. Mao Zhang, L. Li Zhang, Y. Xin Zhang, Hierarchical Cu 2 O/CuO/Co 3 O 4 core-shell nanowires: synthesis and electrochemical properties, Nanotechnology 26 (2015) 304002. https://doi.org/10.1088/0957-4484/26/30/304002.

[104] M. Yu, X. Li, Y. Ma, R. Liu, J. Liu, S. Li, Nanohoneycomb-like manganese cobalt sulfide/three dimensional graphene-nickel foam hybid electrodes for high-rate capability supercapacitors, Appl. Surf. Sci. 396 (2017) 1816–1824. https://doi.org/10.1016/j.apsusc.2016.11.203.